

The ALMA-CRISTAL survey

Widespread dust-obscured star formation in typical star-forming galaxies at $z = 4 - 6$

Ikki Mitsuhashi,^{1,2} Ken-ichi Tadaki,³ Ryota Ikeda,^{4,2} Rodrigo Herrera-Camus,⁵ Manuel Aravena,⁶ Ilse De Looze,^{7,8} Natascha M. Förster Schreiber,⁹ Jorge González-López,^{10,6} Justin Spilker,¹¹ Roberto J. Assef,⁶ Rychard Bouwens,¹² Loreto Barcos-Munoz,^{13,14} Jack Birkin,¹¹ Rebecca A. A. Bowler,¹⁵ Gabriela Calistro Rivera,¹⁶ Rebecca Davies,^{17,18} Elisabete Da Cunha,^{18,19} Tanio Díaz-Santos,^{6,20,21} Andrea Ferrara,²² Deanne Fisher,¹⁷ Lilian L. Lee,⁹ Juno Li,^{18,19} Dieter Lutz,⁹ Monica Relaño,^{23,24} Thorsten Naab,²⁵ Marco Palla,^{26,7} Ana Posses,⁶ Manuel Solimano,⁶ Linda Tacconi,⁹ Hannah Übler,^{27,28} Stefan van der Giessen,^{7,12,25} and Sylvain Veilleux²⁹

(Affiliations can be found after the references)

Received -; accepted -

ABSTRACT

We present the morphological parameters and global properties of dust-obscured star formation in typical star-forming galaxies at $z = 4-6$. Among 26 galaxies composed of 20 galaxies observed by the Cycle-8 ALMA Large Program, CRISTAL, and six galaxies from archival data, we have individually detected rest-frame $158\mu\text{m}$ dust continuum emission from 19 galaxies, nine of which are reported for the first time. The derived far-infrared luminosities are in the range $\log_{10} L_{\text{IR}} [L_{\odot}] = 10.9-12.4$, an order of magnitude lower than previously detected massive dusty star-forming galaxies (DSFGs). The average relationship between the fraction of dust-obscured star formation (f_{obs}) and the stellar mass is consistent with previous results at $z = 4-6$ in a mass range of $\log_{10} M_{\star} [M_{\odot}] \sim 9.5-11.0$ and show potential evolution from $z = 6-9$. The individual f_{obs} exhibits a significant diversity, and it shows a correlation with the spatial offset between the dust and the UV continuum, suggesting the inhomogeneous dust reddening may cause the source-to-source scatter in f_{obs} . The effective radii of the dust emission are on average ~ 1.5 kpc and are ~ 2 times more extended than the rest-frame UV. The infrared surface densities of these galaxies ($\Sigma_{\text{IR}} \sim 2.0 \times 10^{10} L_{\odot} \text{ kpc}^{-2}$) are one order of magnitude lower than those of DSFGs that host compact central starbursts. On the basis of the comparable contribution of dust-obscured and dust-unobscured star formation along with their similar spatial extent, we suggest that typical star-forming galaxies at $z = 4-6$ form stars throughout the entirety of their disks.

Key words. galaxies:high-redshift – galaxies: ISM – dust, extinction

1. Introduction

In recent decades, star formation activity of galaxies at $z \gtrsim 4$ has been progressively studied through their rest-frame ultraviolet (UV) emissions (e.g., Steidel et al. 1999; Daddi et al. 2004; Bouwens et al. 2004b, 2007). Because the rest-frame UV continuum emission traces massive young stars that have a short (~ 100 Myr) lifetime, they are used to estimate star formation rates (SFRs) through the empirical relations (e.g., Kennicutt 1998; Kennicutt & Evans 2012). The *Hubble Space Telescope* (*HST*) provides us with high spatial resolution images covering the rest-frame UV emissions of galaxies at $z \gtrsim 4$. The spatial extent of the star formation is a fundamental parameter for studying galaxy evolution (e.g., Shen et al. 2003), and has been actively explored since the advent of the *HST* (e.g., Lilly et al. 1998; Bouwens et al. 2004a; Ferguson et al. 2004; Daddi et al. 2005; Trujillo et al. 2006; Toft et al. 2007). One of the most surprising results from these studies is that the rest-frame UV effective radii of galaxies decreases with increasing redshift (e.g., Hathi et al. 2008; Oesch et al. 2010; van der Wel et al. 2014; Shibuya et al. 2016).

The UV emission is highly sensitive to absorption by interstellar dust, and the absorbed energy is re-emitted as thermal dust continuum radiation at far-infrared (FIR) wavelengths. Therefore, dust continuum emission is an important tracer to study obscured star formation. In the past decade, Atacama Large Millimeter/Sub-Millimeter Array (ALMA) observations have provided valuable insights into the spatially-resolved properties of high-redshift galaxies, helping us to understand the un-

derlying physical mechanisms driving their morphological evolution. For instance, submillimeter morphologies of dusty star-forming galaxies (DSFGs) have been well-explored thanks to the high spatial resolution achieved with ALMA (e.g., Ikarashi et al. 2015; Hodge et al. 2016; Fujimoto et al. 2017; Gullberg et al. 2019). DSFGs show intense dust-obscured star formation (Casey et al. 2014, , for review). The observed compact star-forming region compared with the stellar distribution (e.g., Chen et al. 2015; Tadaki et al. 2020a) suggest that they are in process of the forming bulge (e.g., Simpson et al. 2015; Nelson et al. 2019; Ikeda et al. 2022) or to be progenitor of compact quiescent galaxies (Toft et al. 2014; Barro et al. 2016). The exploration of DSFGs at $z < 3$ is critical as dust obscures the majority of star formation activity within the redshift range of $1 < z < 3$ (Magnelli et al. 2009, 2011; Moutard et al. 2020).

At redshift exceeding $z > 3$, dust-obscured star formation may also be significant, (e.g., Rowan-Robinson et al. 2016; Gruppioni et al. 2020; Algera et al. 2023) although it has remained uncertain despite extensive efforts (e.g., Bouwens et al. 2012; Dudzevičiūtė et al. 2020; Zavala et al. 2021; Casey et al. 2021; Fujimoto et al. 2023). Recent ALMA deep observations have been used to study the dust-obscured star formation activity of galaxies at $z \gtrsim 4$, which are originally selected by their bright UV emissions (e.g., Watson et al. 2015; Laporte et al. 2017; Fujimoto et al. 2020; Bakx et al. 2021; Laporte et al. 2021; Fudamoto et al. 2021; Schouws et al. 2022). Owing to negative K -correction and the redshift evolution of the dust temperature (T_{dust}) and star formation activities (e.g., Schreiber et al. 2018; Speagle et al. 2014), it is possible to detect dust continuum

emission from galaxies at higher redshift in the frequency coverage of ALMA (see [Blain et al. 2002](#); [Casey et al. 2014](#)). The dust continuum detection of relatively low-mass galaxies such as $M_* \sim 10^{10} M_\odot$ have been increased especially at $z \gtrsim 4$ (e.g., [Watson et al. 2015](#); [Laporte et al. 2017](#); [Bowler et al. 2018](#); [Bakx et al. 2021](#); [Laporte et al. 2021](#); [Fudamoto et al. 2021](#); [Bowler et al. 2022](#); [Schouws et al. 2022](#); [Inami et al. 2022](#); [Bouwens et al. 2022](#); [Ferrara et al. 2022](#); [Sommovigo et al. 2022b](#)). [Inami et al. \(2022\)](#) found that a significant fraction of the star formation activity in bright Lyman-break galaxies with the stellar mass of $M_* \sim 10^{9.5} M_\odot$ at $z \sim 7$ is obscured by dust (see also [Bouwens et al. 2022](#); [Ferrara et al. 2022](#); [Sommovigo et al. 2022b](#); [Algera et al. 2023](#)), consistent with predictions from cosmological galaxy simulations (e.g., [Cullen et al. 2017](#)).

Since the individual detection of the dust continuum from $z \gtrsim 4$ galaxies, there have been extensive efforts to understand the role of dust-obscured star formation in the internal structure of UV-bright galaxies. For instance, [Bowler et al. \(2022\)](#) revealed the spatial correlation between dust continuum detection and redder colors (see also, [Bowler et al. 2018](#)). However, spatially-resolved observations of dust emission from the galaxies with $M_* \sim 10^{10} M_\odot$ remain challenging even with ALMA (e.g., [Fujimoto et al. 2020](#); [Ginolfi et al. 2020a](#); [Inami et al. 2022](#); [Hygate et al. 2023](#)) and are still limited (e.g., [Herrera-Camus et al. 2021](#); [Béthermin et al. 2023](#); [Devereaux et al. 2023](#)).

In this paper, we investigate dust-obscured star formation activity and the spatial extent of dust emission in 26 normal, representative star-forming galaxies at $z = 4-6$ by utilizing data from the ALMA Large Program, [C II] Resolved ISM in STar-forming galaxies with ALMA (CRISTAL) and some archival data. With the ancillary data set including deep *HST* images, we examine distributions of the dust-obscured and unobscured star-forming regions in the early Universe. The paper is organized as follows: Section 2 provides an overview of the CRISTAL survey sample and data products. Section 3 describes the method of size measurements for the ALMA and *HST* data, and reports the results of the size measurements and associated physical properties. In Section 4, we discuss the physical origin of the dust distribution and the morphological evolution of the CRISTAL galaxies. A summary of this study is presented in Section 5. Throughout this paper, we assume a flat universe with the cosmological parameters of $\Omega_M = 0.3$, $\Omega_\Lambda = 0.7$, $\sigma_8 = 0.8$, and $H_0 = 70 \text{ km s}^{-1} \text{ Mpc}^{-1}$.

2. Observation and Data

2.1. The ALMA CRISTAL survey

CRISTAL is an ALMA Cycle-8 large program (2021.1.00280.L; PI: Rodrigo Herrera-Camus, see [Herrera-Camus et al. in prep.](#)). CRISTAL aims to spatially resolve the [C II] line and rest-frame $158\mu\text{m}$ dust continuum emissions of typical star-forming galaxies at $z \sim 4-6$. The parent sample of CRISTAL is composed of 75 galaxies whose [C II] emission is detected in the ALPINE survey (ALMA Large Program to Investigate C⁺ at Early Times; 2017.1.00428.L; PI: O. Le Fèvre [Le Fèvre et al. 2020](#)) with the spatial resolution of $\sim 1''$. For the CRISTAL program, we selected targets based on spectral energy distribution (SED) modeling with LEPHARE ([Faisst et al. 2020b](#); [Béthermin et al. 2020](#)), with the following criteria: (1) the specific SFR is within a factor of 3 from the star formation main sequence at each redshift ([Speagle et al. 2014](#)), (2) *HST* images are available, (3) stellar mass is larger than $\log_{10} M_* [M_\odot] \geq 9.5$. All galaxies are located in the COSMOS or GOODS-S field and $\sim 80\%$ of the galaxies are covered by the ongoing (or planned) *JWST* observations such as the COSMOS-Web treasury program ([Casey et al. 2022](#)), PRIMER program ([Dunlop et al. 2021](#)) or some GTO programs (e.g., ID1286). The mass-selected UV-bright galaxies provide a census of the gas, dust, and stars of typical star-forming galax-

ies on a kiloparsec scale with a combination of high-resolution ALMA and *HST/JWST* observations.

In addition, we added six galaxies in the COSMOS field (HZ4, HZ7, HZ10, DC818760, DC873756, VC8326, see also [Capak et al. 2015](#); [Faisst et al. 2020b](#); [Béthermin et al. 2023](#); [Devereaux et al. 2023](#)) referred to as the CRISTAL+ galaxies (corresponding to CRISTAL-20, 21, 22, 23, 24, 25, respectively) because they have ALMA data with similar spatial resolution and sensitivity as the CRISTAL (2018.1.01359.S and 2019.1.01075.S; PI: Manuel Aravena, 2018.1.01605.S; PI: Rodrigo Herrera-Camus, 2019.1.00226.S; PI: Edo Ibar). Also, we exclude one galaxy (CRISTAL-18) because it does not exhibit clear [C II] and dust continuum detections possibly due to mis-estimation of [C II] frequency. Hence, the CRISTAL extended sample is composed of 24 target fields with available sensitive ALMA [C II] plus dust continuum imaging $\lesssim 0.3''$. Details of the survey design and observation setup are presented in [Herrera-Camus et al. \(in prep.\)](#).

2.2. Properties of the CRISTAL galaxies

To uniformly estimate galaxy-integrated physical properties of the CRISTAL galaxies including several serendipitously detected sources in both [C II] and dust continuum (see Section 3.1), and confirm the robustness of the physical parameter estimations in the individual SED fitting code, we perform multi-wavelength SED fitting using the CIGALE code ([Boquien et al. 2019](#)).

We cross-match positions of the CRISTAL galaxies to publicly available photometric catalogs in COSMOS (COSMOS2015 catalog, [Laigle et al. 2016](#))¹ and GOODS-S fields (ASTRODEEP catalog, [Merlin et al. 2021](#)). All of the CRISTAL galaxies have counterparts within $1''$. The model SEDs are generated with stellar population synthesis models of [Bruzual & Charlot \(2003\)](#) under a [Chabrier \(2003\)](#) initial mass function with a range of $0.1-100 M_\odot$ assuming exponentially declining star formation histories (SFHs). We adopt [Calzetti et al. \(2000\)](#) dust attenuation law and CLOUDY ([Ferland et al. 1998](#)) nebular emission line template. Details of the fitting and parameter range are summarized in the Appendix.

We derive stellar masses and SFRs averaging the SFH over the last 100 Myr (SFR_{SED}) from the best-fit SED models. Figure 1 shows the relation between stellar mass and SFR for the CRISTAL galaxies. We also perform SED fitting for all galaxies at $z = 4-6$ in the COSMOS2015 catalog with the exact same setup as for the CRISTAL galaxies. CRISTAL galaxies have stellar masses of $\log_{10} M_* [M_\odot] \geq 9.5$, which are consistent with the results from LEPHARE code in the ALPINE program within the 1σ uncertainty. A comparison with the star formation main sequence at $z = 5$ ([Speagle et al. 2014](#)) indicates that CRISTAL galaxies are a representative population of star-forming galaxies at this epoch. Note that the estimated parameters of CRISTAL-01 might be uncertain due to the contamination of *Spitzer* band photometry by a nearby bright source (see Figure 1). The stellar mass estimation will be improved by *JWST* data in the future ([Li et al. in prep.](#)) as most of the CRISTAL galaxies have *JWST/NIRCam* coverage as described in Section 2.1. We also note that CRISTAL-24 is located below the main sequence due to small SFR_{SED} . Since SFR estimated from UV and IR radiation ($\text{SFR}_{\text{UV}} + \text{SFR}_{\text{IR}}$) is ~ 1.3 dex higher than SFR_{SED} , SFR_{SED} derived from optical to NIR photometry appears to be underestimated due to the degeneracy of dust extinction and stellar age (see Figure B.1). The stellar masses and SFRs for the CRISTAL galaxies are summarized in [Herrera-Camus et al. \(in prep.\)](#).

¹ We find there are spatial offsets between the detected position in the COSMOS2015 catalog and the latest the COSMOS catalog ([Weaver et al. 2022](#)). For our target galaxies, COSMOS2015 catalog shows better identifications.

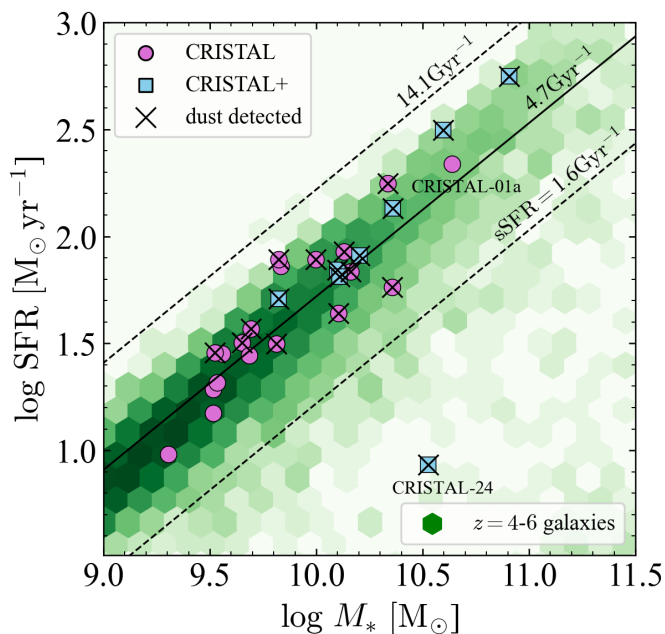


Fig. 1. SFR vs stellar mass with $z = 5$ main-sequence parameterization (Speagle et al. 2014) and comparison $z = 4-6$ galaxies in the COSMOS catalog (Laigle et al. 2016). Pink squares are primary targets of the CRISTAL program and blue squares are serendipitously detected galaxies and additional CRISTAL+ galaxies (see Section 2.1). The sources whose dust continuum is detected with $S/N > 4$ are marked with crosses. The CRISTAL galaxies are located within ± 0.5 dex of the star formation main sequence at $z = 5$, suggesting they are representative populations at this epoch.

2.3. Observation and Data products

CRISTAL observations cover a wide range of spatial frequencies in the uv plane with a combination of extended (C43-4/5/6) and compact (C43-1/2) array configurations to achieve not only high-resolution ($\sim 0.3''$, corresponding to ~ 1.9 kpc in physical scale at $z = 5$) but also a large maximum recoverable scale ($\sim 4.5''$, corresponding to ~ 28.3 kpc in physical scale at $z = 5$). We determine the spectral frequency coverages by centering [C II] frequency derived from the integrated [C II] spectral line profile in the ALPINE survey. Observations were carried out from November 2021 to April 2023. Details of the calibration, reduction, and data products will be presented in Herrera-Camus et al. (in prep).

In addition to the CRISTAL observations taken in two array configurations, all CRISTAL galaxies have archival observations (2012.1.00978.S, 2012.1.00523.S, and 2017.1.00428.L). As these archival data typically cover shorter spatial frequency ranges in the uv plane compared with the CRISTAL observations, adding these archival data improves the sensitivities, especially to extended emissions. We use the archive data by combining visibilities with the CASA/CONCAT task.

3. Analysis and Results

3.1. Dust continuum detected galaxies

In this paper, we focus on the dust continuum emission of CRISTAL galaxies. We exclude visibility data in the frequency range corresponding to the [C II] emission line. To ensure avoiding the contamination of [C II] lines to the dust continuum, we exclude ± 0.45 GHz, which correspond to ± 400 km s^{-1} and ± 450 km s^{-1} for $z = 4.5$ and 5.5 respectively, from the [C II] central frequencies since broad component of [C II] emission lines could reach ~ 250 km s^{-1} in FWHM/2 (Ginolfi et al.

2020b). Next, we make multi-frequency synthesis (continuum) images with CASA task `TCLEAN` to look at their signal-to-noise ratio (S/N). Here we did not apply `CLEAN` algorithm (i.e., dirty images) and primary beam correction to perform a consistent comparison between noises and signals (c.f., JvM correction, Czekala et al. 2021, Gonzalez-Lopez et al. in prep). To avoid low S/N for extended emission in galaxies and investigate how well the extended emission of galaxies is recovered, we create low-resolution images with uv taper of $0.25''$, $0.5''$, $1.0''$, and $2.0''$ as well as high-resolution images with natural weighting. In all images with different resolutions, we pick maximum fluxes in dust continuum images within a circle of radius $0.5''$ around the position of previous [C II] detection. The noise is estimated by calculating 3σ clipped root-mean-square (RMS) values of all pixels within the Field-of-View (FoV) where the primary beam correction value is between 0.9 and 0.5 to avoid the impact of the target galaxy for sure. Typical RMSs are $10-20 \mu\text{Jy beam}^{-1}$.

In the vicinity of the main targets, we serendipitously found 2 sources with $> 8\sigma$ [C II] detection, $> 4\sigma$ dust continuum detection, and *HST* detection (CRISTAL-01b and 07c). We include these galaxies in the main analysis. Please refer to Herrera-Camus et al. (in prep) for more detail on serendipitous [C II] and dust detections around CRISTAL galaxies. In a total of 26 extended CRISTAL samples (18 original CRISTAL targets, 6 CRISTAL+ galaxies, and 2 serendipitously detected galaxies in original CRISTAL fields), we found that 7, 8, and 11 galaxies have dust continuum emissions with $S/N < 4$, $4 \leq S/N < 6.5$, and $S/N \geq 6.5$ respectively.

We show thumbnails of the dust-detected CRISTAL galaxies in Figure 2. The dust-detected galaxies tend to have higher stellar masses ($\log_{10} M_* [M_\odot] \geq 9.7$) and SFRs ($\log_{10} \text{SFR} [M_\odot \text{yr}^{-1}] \geq 1.5$). The median stellar mass and SFR of the dust-detected and undetected sample are $\log_{10} M_* [M_\odot] = 10.1$, $\log_{10} \text{SFR} [M_\odot \text{yr}^{-1}] = 1.8$ and $\log_{10} M_* [M_\odot] = 9.5$, $\log_{10} \text{SFR} [M_\odot \text{yr}^{-1}] = 1.4$, respectively. The detection rate is 89% (16/18) in a stellar mass range of $\log_{10} M_* [M_\odot] > 9.7$ (Figure 1). Our detections of faint galaxies in the dust continuum down to the stellar mass of $M_* \sim 10^{9.5} M_\odot$ provide new insight into the dust-obscured star formation activities of less massive galaxies.

3.2. Dust size measurement

In this section, we characterize the spatial extent of the rest-frame $158 \mu\text{m}$ dust continuum emissions in the CRISTAL galaxies. In principle, it is possible to measure the size of galaxies by deconvolving an image with a clean beam. However, reconstructed images through the Fourier transform of the visibility data and non-linear `CLEAN` algorithm strongly depend on the uv coverage of visibilities and its weight, which could lead to systematic uncertainties. Moreover, as about one-third of CRISTAL galaxies lack high S/N ($S/N \geq 5$) in the dust continuum images, image-based analysis may make measurements uncertain. To achieve homogenous size measurements and to utilize full information from the observations, we directly measure the effective radii of dust continuum emission from the visibility data.

Recent high-resolution ALMA observations revealed that DSFGs are generally consistent with Sérsic profile (Sérsic 1963) with the index of $n \sim 1$ (e.g., Hodge et al. 2016; Gullberg et al. 2019). Even for fainter sources, Tadaki et al. (2020a) suggest that their surface density profiles are better characterized by an exponential profile with $n = 1$ than a Gaussian profile with $n = 0.5$. Therefore we fit a 2D exponential profile ($n = 1$) by using UV-MULTIFIT (Martí-Vidal et al. 2014).

The observed visibilities are presented as a combination of amplitude and phase from all sources within the FoV. Hence, to extract information specific to the target galaxy, it is necessary to subtract contributions from other continuum sources within

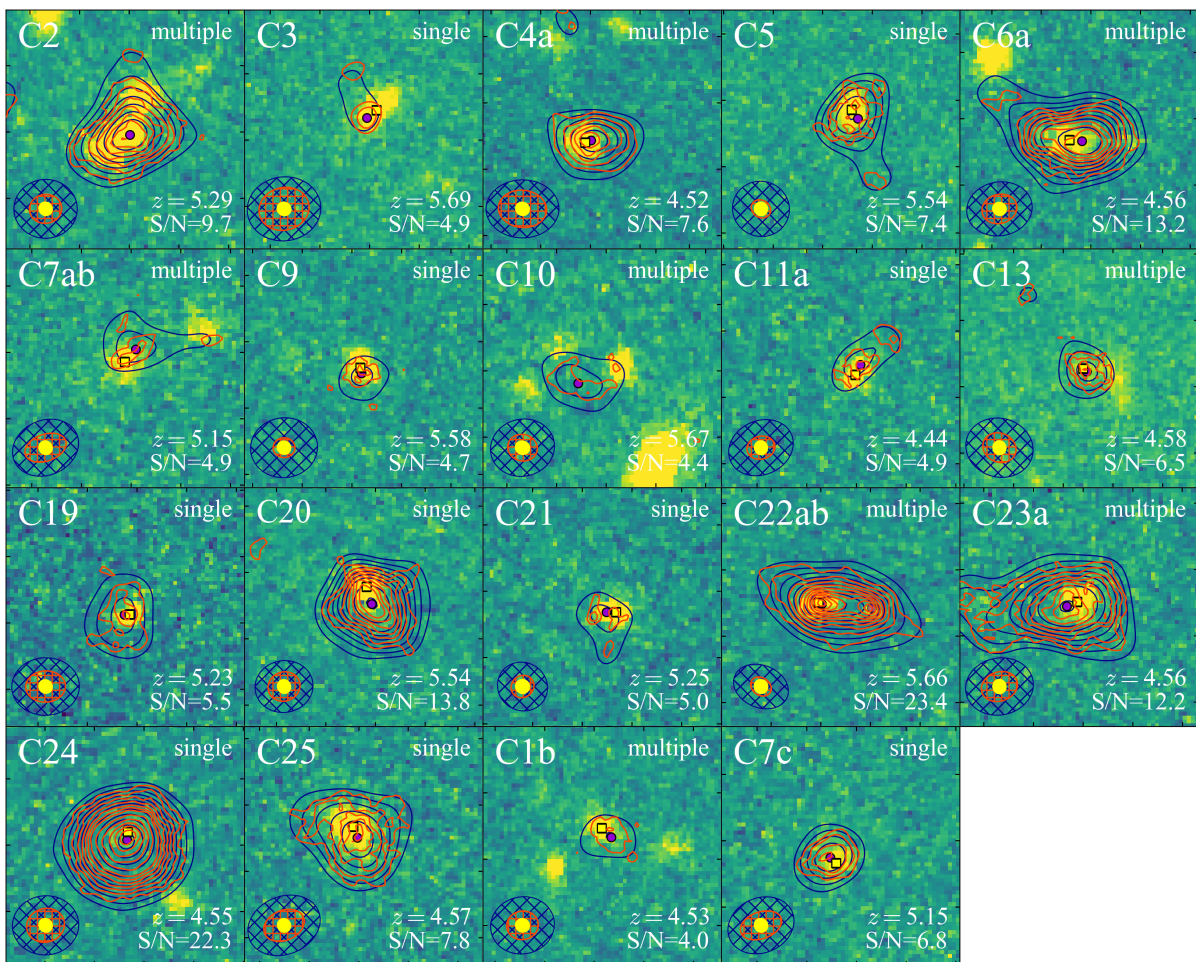


Fig. 2. Thumbnails of the dust detected CRISTAL galaxies. The background images are *HST*/F160W images. The natural-weighted and natural-weighted+0.5''-Tapered rest-frame 158 μm dust continuums are also shown in red and blue contours, respectively. An average beam size of natural-weighted continuum images is $0.46'' = 2.9 \text{ kpc}$. The contour levels are shown every 1σ within $3\text{--}9\sigma$ and every 2σ from 9σ , respectively. For CRISTAL-22, for every 2σ from 3σ . The source ID, redshift, S/N, and morphological classification based on the *HST* images are also shown in each panel.

the FoV especially when they are close to the target. Sources more than $2''$ apart from the target galaxy are subtracted using the CASA `TCLEAN` task. We clean down to 1.5σ by applying $2''$ masks from the source position to extract the clean component of the nearby sources and subtract them from the observed visibilities with CASA task `UVSUB`. Note that there is no significant difference if we conduct the two-component fitting to take into account the other continuum sources. When we clearly find the existence of a second component in the residual map after subtracting the best-fit single component with $S/N > 10$ (CRISTAL-22), we use the results of the two-component fitting. As the CRISTAL galaxies typically do not have high S/N ($S/N > 5$) in the dust emission (Table 1), the axis ratio (q) is not well constrained in most galaxies. Thus, we measure the effective radii of the dust emission by assuming a circular exponential disk with a fixed value of $q = 0$. We create residual maps from the visibilities where the best-fit model is subtracted in the uv plane.

Figure 3 shows an example of a dirty map, a residual map, and a real part of the observed visibilities as a function of uv distance. Because there is no peak above $\sim 3\sigma$ in the residual maps, the exponential disk model seems to successfully represent the spatial distribution of dust emission. Thanks to the observations in the extended array configurations, we successfully capture a decline of the real part of the visibilities that clearly suggests the dust continuum from the source is spatially resolved. A signal at

the real part with increasing uv distance is the reciprocal of the spatial extent at an image plane since the Fourier transform of the profile in the image plane is a profile in the visibility plane. All of the original, model, and residual maps are shown in the Appendix.

To check the goodness of the visibility fitting, we compare the flux densities of dust continuum emission estimated from the visibility fitting and those from the low-resolution image (Figure 4). Here we make the images with a beam size of $3.0''$ by applying CASA/`IMSMOOTH` to the $2.0''$ -tapered images to transform the resolution of each source to a common beam size and to make sure that all of the flux densities are included within a single beam. Then we measured source flux densities with the same method used in Section 3.1. We find the visibility fitting recovers the flux densities well in various sources from the brightest to the faintest among the CRISTAL galaxies, except for a very extended source (CRISTAL-21). The inconsistency of flux densities in CRISTAL-21 likely originates from extrapolation of the best-fit model toward the short uv distance regime due to a low sensitivity at $\leq 50 \text{ k}\lambda$. When the additional $2''$ -taper is applied to CRISTAL-21, we find a better match with the visibility-based estimation. To maintain consistency between the detected and undetected galaxies in the dust continuum, hereafter we use the flux densities and 1σ uncertainties estimated from the low-resolution (i.e., tapered) images.

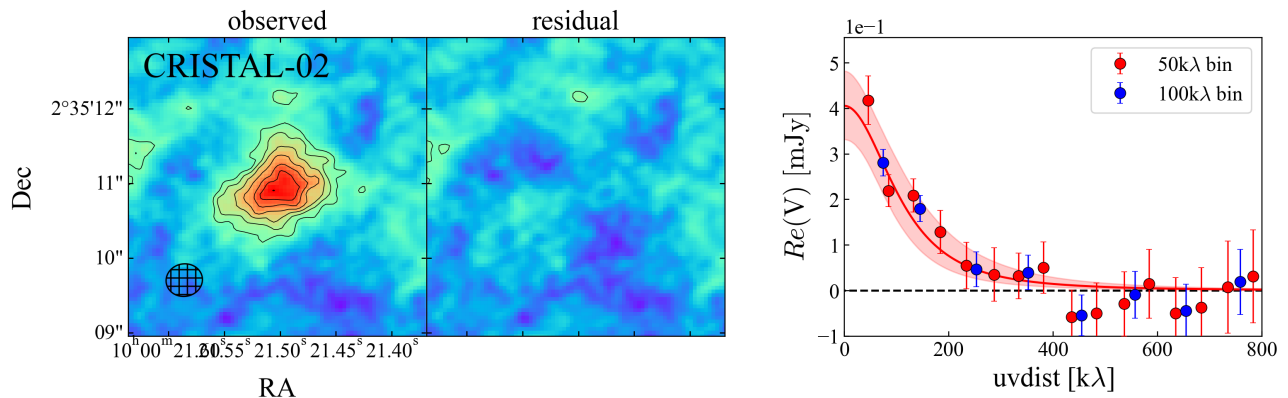


Fig. 3. An example of the fitting in the visibility plane. **left:** The observed and residual (observed - best-fit model) dirty map of the dust continuum emission. The synthesized beam is shown in the bottom left. The black contour shows every 1σ from $\pm 3\sigma$. **right:** The real part of the observed visibilities as a function of uv distances with different binning scales. The best-fit exponential disk model and its 1σ uncertainty are shown in a red solid line and shaded area respectively.

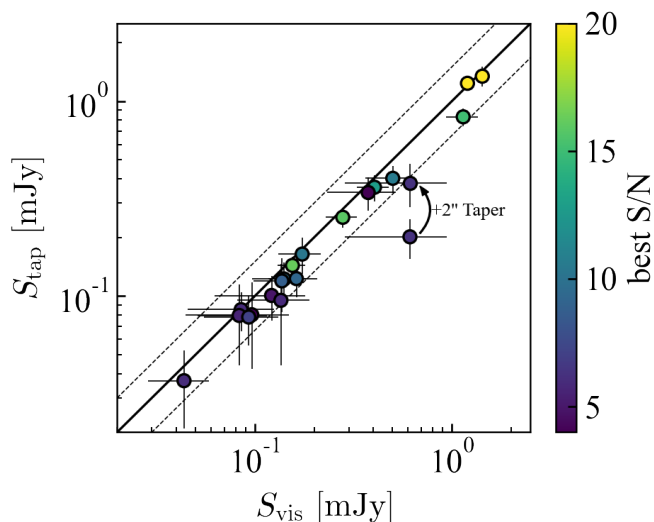


Fig. 4. Comparison of the flux density estimated from UVMULTIFIT and Taper images, color-coded by the source S/N. The black solid line and dashed lines indicate a one-to-one relation and ± 0.3 dex. We see the visibility fitting recovered the fluxes of the sources in lower resolution images well within the $1-\sigma$ errors, except for CRISTAL-21 (see text).

We summarize the fluxes measured in visibilities via UVMULTIFIT and low-resolution images in Table 1. Since about half of the CRISTAL galaxies range $4.4 < S/N < 5.5$ in the dust continuum images (see Table 1), we conduct a Monte Carlo simulation and a stacking analysis to confirm the validity of the size measurement in Appendix. We do not find any systematic offset regardless of the source S/N in the Monte Carlo simulation and there is no clear difference between the stacked size and the average of the individual sizes in the stacking analysis. Therefore we conclude that the fitting results are reliable.

3.3. FIR luminosity

Because most of the CRISTAL galaxies have only single band ALMA detections in the dust continuum, it is not possible to estimate properties such as dust temperature (T_{dust}) and emis-

sivity (β_{dust}), which are crucial in determining the shape of the FIR SED. Béthermin et al. (2017) presented best-fit Draine & Li (2007) dust emission model for stacked fluxes of the main-sequence galaxies at $z \sim 4$ with *Spitzer*, *Herschel*, LABOCA, and AzTEC data (see also Béthermin et al. 2015). This best-fit FIR SED agrees with the stacked fluxes of $z = 4-6$ main-sequence galaxies with $\text{SFR}_{\text{SED}} > 10 M_{\odot} \text{yr}^{-1}$ (Béthermin et al. 2020), corresponding to the modified blackbody with the dust temperature $T_{\text{dust}} \sim 42$ K. Indeed, some CRISTAL galaxies have rest-frame 110 and 200 μm observations and show a consistent T_{dust} estimation with the assumption of $T_{\text{dust}} \sim 42$ K (Faisst et al. 2020a), while there exists a variation in the FIR SED with the range of dust temperatures of $T_d \sim 30-60$ K. Sommovigo et al. (2022a) apply the physically-motivated model to characterize T_{dust} validated in Sommovigo et al. (2021) for the $z \sim 5$ galaxies that is partly overlapping with the CRISTAL galaxies. The derived average T_{dust} is 48 ± 8 K, and is broadly consistent with the assumption of 42 K. Because our CRISTAL galaxies share similar SFRs with the galaxies studied in Béthermin et al. (2020), we use the best-fit FIR SED presented in Béthermin et al. (2017) to estimate the total IR (8–1000 μm) luminosities of the CRISTAL galaxies. We calculate the total FIR luminosities of the CRISTAL galaxies by converting the measured dust continuum fluxes at the rest-frame 158 μm using a scaling factor described Béthermin et al. (2020, $\nu L_{\nu=158\mu\text{m}}/L_{\text{IR}} = 0.133$). The resulting L_{IR} of CRISTAL galaxies fall within a range of $\log_{10} L_{\text{IR}} [L_{\odot}] = 10.9-12.4$.

Figure 5 shows the total infrared luminosity against the circularized effective radius (left) or the surface infrared luminosity $\equiv \Sigma_{\text{IR}} = L_{\text{IR}}/2\pi r_{e,\text{dust}}^2$ (right) of dust continuum emission. As a comparison, we show the results of different galaxy populations, namely sub-millimeter galaxies (SMGs) at $z \sim 2.5$ (Gullberg et al. 2019), lensed SMGs at $z \sim 3-6$ (Spilker et al. 2016), DSFGs at $z = 4-6$ (Riechers et al. 2014; De Breuck et al. 2014; Hodge et al. 2015; Gómez-Guijarro et al. 2018; Casey et al. 2019; Tadaki et al. 2020b) and DSFGs at $z \sim 2$ (Tadaki et al. 2020a). The comparison galaxies are mainly starburst galaxies above the main sequence at the corresponding epochs, and their FIR luminosities are derived by some templates of FIR SEDs (e.g., Wuyts et al. 2008; da Cunha et al. 2015) or modified blackbody fitting with the typical dust temperature $T_{\text{dust}} = 30-50$ K. Solid and dashed lines indicate a series of r_e and L_{IR} each cor-

responding to the median infrared surface densities (Σ_{IR}) of the respective sample, as indicated by the matching color.

The median values of Σ_{IR} are $2.0 \times 10^{12} L_{\odot} \text{ kpc}^{-2}$ for lensed SMGs, $9.8 \times 10^{11} L_{\odot} \text{ kpc}^{-2}$ for SMGs at $z \sim 2.5$, $1.6 \times 10^{12} L_{\odot} \text{ kpc}^{-2}$ for SMGs at $z = 4-6$, and $1.6 \times 10^{11} L_{\odot} \text{ kpc}^{-2}$ for DSFGs at $z = 2$. The median Σ_{IR} of the CRISTAL galaxies is $2.0 \times 10^{10} L_{\odot} \text{ kpc}^{-2}$ and ~ 10 times smaller than that of the central compact star-forming regions of DSFGs or SMGs (Figure 5 right), and similar to that of the extended dust continuum component of the SMGs reported in the stacked spatial distribution (Gullberg et al. 2019, $\Sigma_{\text{IR}} \sim 5 \times 10^{10} L_{\odot} \text{ kpc}^{-2}$) that is considered to be disk components. Our representative population of galaxies at $z \sim 4-6$ seems to undergo moderate star formation with a lower Σ_{IR} than those of DSFGs, except for some galaxies (CRISTAL-22 and 24) showing the high Σ_{IR} those are comparable with DSFGs and SMGs. Interestingly, Ferrara et al. (2022) analytically derive the L_{IR} and dust distribution radius of the REBELS (Reionization Era Bright Emission Line Survey; Bouwens et al. 2022) galaxies at $z \sim 7$. They find a more compact distribution ($r_d \sim 0.3 \text{ kpc}$) and a similar L_{IR} with the CRISTAL galaxies ($\log_{10} L_{\text{IR}} [L_{\odot}] \sim 11.8$), which results in a higher Σ_{IR} ($\log_{10} \Sigma_{\text{IR}} [L_{\odot} \text{ kpc}^{-2}] \sim 12.1$) than our measurements. Direct measurement of the dust continuum distribution by the future ALMA high-resolution observations for $z > 6$ galaxies will enable us to compare our results with that of the galaxies at $z > 6$.

3.4. Rest-frame UV size measurement

To compare the spatial extent of the dust-obscured and unobscured star formation, we measure the rest-frame UV sizes of the CRISTAL galaxies. In this section, we summarize the size measurements of the rest-frame UV emission observed with *HST*.

Because all of the CRISTAL galaxies have WFC3/F160W coverage and $1.6 \mu\text{m}$ corresponds to rest-frame $\sim 2400-3000 \text{ \AA}$ in the redshifts of the CRISTAL galaxies ($z = 4.4-5.7$), we constantly use images from WFC3/F160W observation to measure the rest-frame UV sizes of the CRISTAL galaxies.

We measure the *HST* size based on two-dimensional (2D) surface-brightness profile fitting with GALFIT (Peng et al. 2002). First, we make a point-spread function (PSF) in the same manner as previous studies (e.g., Skelton et al. 2014). We selected point sources (i.e., stars) based on the following criteria: (1) ratios of fluxes with $2.0''$ apertures and $0.5''$ apertures are in a range of 1.2 and 1.4 based on the tight flux correlation in the point source. (2) S/Ns are greater than 7500. We exclude the point sources if they have nearby sources within $3''$. Because the central position of the point source does not necessarily correspond to the central position of the pixel, we reproject the 2D point source profile with a linear interpolation to the central position derived from 2D Gaussian fitting. Then we obtain the PSF by stacking these reprojected stellar profiles after normalizing with the total flux of each source. We also create *sigma* and *mask* images to estimate the weight of individual pixels and exclude neighboring objects of the target galaxy from the fittings. The *sigma* images are made from drizzle weight maps and *mask* images are produced from segmentation maps from SEXTRACTOR with a parameters of DETECT_MINAREA=5, DETECT_THRESH=2, DETECT_NTHRESH=16 and DEBLEND_MINCONT=0.0001. We input the *sigma*, *mask*, and PSF to GALFIT and fit a single Sérsic profile to the 2D surface-brightness profile of each galaxy. Here we fix $n = 1$ to perform fair comparisons with the dust size measurement. Note that there is no systematic difference if we do not fix the Sérsic index except for CRISTAL-25, showing a large Sérsic index in the best-fit model (see Figure D.1). Finally we obtain an effective radius along the major axis $r_{e,\text{UV}}^{\text{major}}$ and axis ratio q , and convert them to the circularized effective radius $r_{e,\text{UV}}$ through

$r_{e,\text{UV}} \equiv r_{e,\text{UV}}^{\text{major}} \sqrt{q}$. If the fitting does not converge with the axis ratio as a free parameter, we fix the axis ratio to unity as in the size measurement in the dust continuum. The original, model, and residual maps are shown in Appendix. For CRISTAL-22, we only measure the size of the main component by masking the second component because the latter is too faint and the fitting does not converge (see Figure 2).

In Figure 6, we compare measured sizes of the dust-obscured star formation derived from rest-frame $158 \mu\text{m}$ dust continuum observations by ALMA and the dust-unobscured star formation derived from rest-frame UV continuum observations by *HST*/WFC3 F160W. The dust-obscured star formation appears to be on average ~ 2 times more spatially extended than the dust-unobscured star formation. We discuss the spatial extent of the dust and UV emissions in Sec 4.3.1.

The measured dust and rest-frame UV sizes are summarized in Table 1.

4. Discussion

4.1. Fraction of obscured star formation

The obscured fraction of star formation (f_{obs}) is defined by the ratio of the dust-obscured star formation detected in rest-frame IR continuum emission to the total star formation rates accounting for dust-unobscured star formation observable in rest-frame UV continuum emission as following:

$$f_{\text{obs}} = \frac{\text{SFR}_{\text{IR}}}{\text{SFR}_{\text{UV}} + \text{SFR}_{\text{IR}}} \quad (1)$$

In general, the obscured fractions show a positive correlation with the stellar masses of the galaxies (e.g., Whitaker et al. 2017; Reddy et al. 2018) as well as some studies presenting the same trend in IR excess (IRX; $\log_{10} L_{\text{IR}}/L_{\text{UV}}$), which is a similar quantity with f_{obs} as an indicator of the obscured star formation (e.g., Pannella et al. 2009, 2015; Bouwens et al. 2016; Dunlop et al. 2017; McLure et al. 2018; Bouwens et al. 2020). Based on the results in Whitaker et al. (2017), the obscured fractions do not exhibit any clear evolution from $z \sim 2.5$ to $z \sim 0$ in the average obscured fraction of $f_{\text{obs}} = 0.8$ (for Dale & Helou 2002 template) or 0.6 (for Magdis et al. 2012 and Béthermin et al. 2015 template). Recent ALMA studies suggest a possible decrease in the mass dependence of f_{obs} at a high mass range ($M_* \gtrsim 10^{10} M_{\odot}$) at $z > 4$ (Fudamoto et al. 2020b,a; Inami et al. 2022; Algera et al. 2023).

In order to confirm if similar trends can be observed in our data, we calculate the average obscured fraction of the sample binned by their stellar masses. We divide the sample into three ranges with $\log_{10} M_* [M_{\odot}] = [9.3 : 9.8]$, $[9.8 : 10.2]$ and $[10.2 : 10.9]$ so that the number of galaxies in each bin is similar. For the stacking analysis, we make the images with the taper scale of $2''$ after shifting the phase center of the image to the central position of the [C II] emission (Ikeda et al. in prep.). Then we apply the CASA/IMSMOOTH to unify the beam size to $3''$ following the flux measurements in Section 3.2 and perform median stacking of the images. We take into account the redshift difference of the target galaxies by multiplying the factor of $(1+z)/d_L^2$ to the image because our calculation from $S_{158\mu\text{m}}$ to L_{IR} is proportional to the reciprocal of the factor. Note that the offset between the dust continuum and [C II] emission does not impact the result because the typical offset ($\sim 0.2''$) is much smaller than $3''$ beam size. We confirm that the results do not change significantly if we adopt the inverse L_{UV} weight following Fudamoto et al. (2020a). The infrared luminosity is derived from a peak flux of the dust continuum as in section 3. We calculate the median L_{UV} of the galaxies obtained from the best-fit SEDs in each bin. Then we convert them into SFR_{UV} or SFR_{IR} following Madau & Dickinson (2014). Figure 7 (left) illustrates the average f_{obs} in each

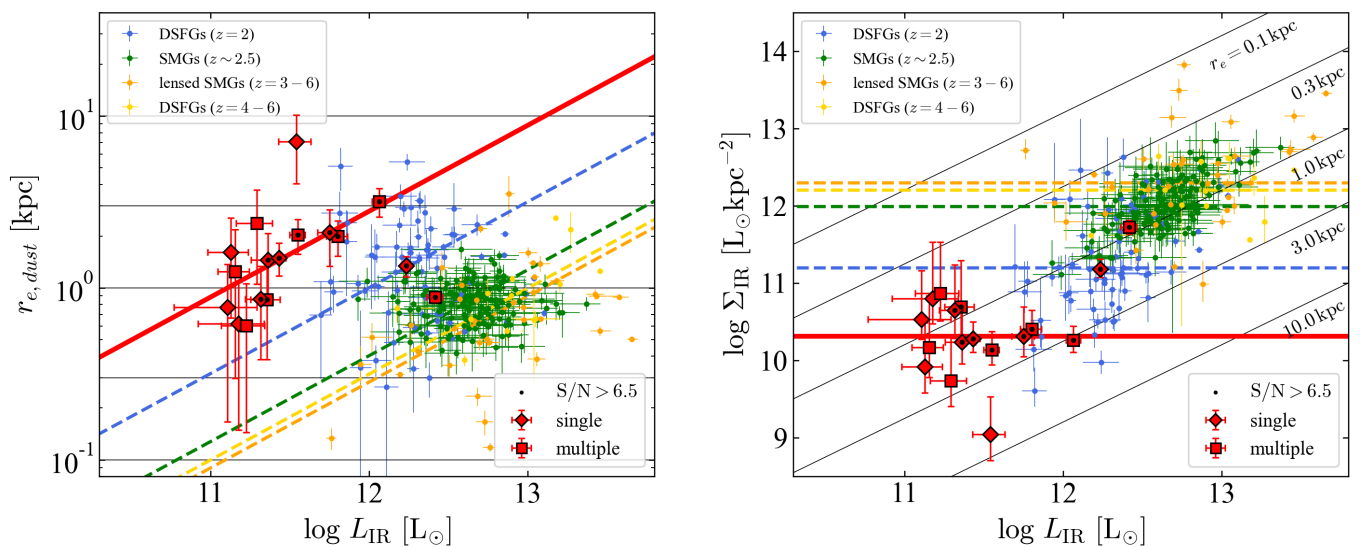


Fig. 5. Total infrared luminosities and **(left)** effective radii and **(right)** surface infrared luminosities for CRISTAL galaxies, SMGs at $z \sim 2.5$ (Gullberg et al. 2019), lensed SMGs at $z \sim 3-6$ (Spilker et al. 2016), SMGs at $z = 4-6$ (Riechers et al. 2014; De Breuck et al. 2014; Hodge et al. 2015; Gómez-Guijarro et al. 2018; Casey et al. 2019; Tadaki et al. 2020b) and DSFGs at $z \sim 2$ (Tadaki et al. 2020a). Solid and dashed lines show the median Σ_{IR} for each sample. CRISTAL galaxies show ~ 10 times smaller Σ_{IR} than that of DSFGs or SMGs, and are less extreme galaxies compared with DSFGs.

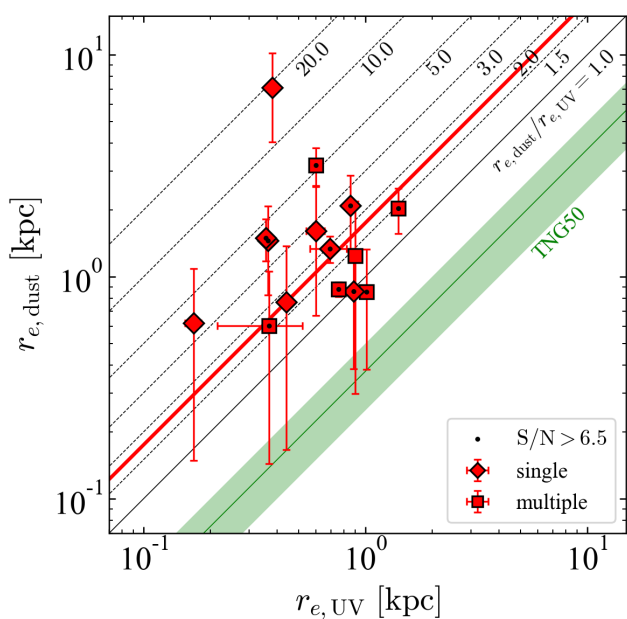


Fig. 6. Size comparison of the dust continuum ($r_{e,\text{dust}}$) and the UV continuum ($r_{e,\text{UV}}$). The black solid and dashed lines indicate the size ratios of the UV and dust continuum. An average size ratio of the CRISTAL galaxies ($r_{e,\text{dust}}/r_{e,\text{UV}} \sim 1.8$) are shown in the red solid line. The green shaded region shows the size ratio predicted in illustrious TNG50 simulation (Popping et al. 2022). Overall, CRISTAL galaxies possibly have a more extended distribution in dust thermal emission than in UV radiation, and it is contrary to the expectation from the simulation.

stellar mass bin ($f_{\text{obs}}-M_*$). Our results support that the obscured fraction at the range of $M_* < 10^{10} M_{\odot}$ does not show clear evolution from $z = 0-2.5$ (Magdis et al. (2012) and Béthermin et al. (2015)) to $z \sim 5$. On the other hand, we find the possible evolution of the obscured fraction from $z \sim 5$ to $z \sim 0-2.5$ at the range of $M_* > 10^{10} M_{\odot}$, and that implies a build-up of dust in massive galaxies. Note that as our sample selection is originally based on

a bright UV continuum and emission lines, it likely led to missing obscured dusty galaxies (e.g., Franco et al. 2018; Yamaguchi et al. 2019). We find our results have a very good agreement with the results at $z = 4.5$ and $z = 5.5$ from the ALPINE survey (Fudamoto et al. 2020a), and $z = 6-9$ from the REBELS survey (Algera et al. 2023). Compared with the another results at $z = 6.5-7.7$ from the REBELS survey (Bowler et al. 2023), our results are indicate slightly lower f_{obs} at $M_* < 10^{10} M_{\odot}$. Bowler et al. (2023) discussed that the the effect of scatter in the obscuration or the clumpy morphology of their target galaxies may cause such a difference.

Figure 7 (right) shows the obscured fraction of the individual galaxies as a function of the stellar mass. The CRISTAL galaxies show a large diversity of $f_{\text{obs}} = 0.2-0.9$. Since we utilized the same scaling factor as Fudamoto et al. (2020a) to convert $S_{158\mu\text{m}}$ into L_{IR} (Béthermin et al. 2020), lower values of f_{obs} suggest smaller $S_{158\mu\text{m}}$. Some CRISTAL galaxies show smaller f_{obs} than galaxies individually detected in Fudamoto et al. (2020a), with a median f_{obs} in Fudamoto et al. (2020a) of 0.70 compared to 0.61 in our work, respectively. The smaller values of f_{obs} are consistent with those stacking analyses (Fudamoto et al. 2020a; Algera et al. 2023). By utilizing the coverage of the wide range f_{obs} , we discuss the variation of f_{obs} in the next section.

4.2. Origin of the spread in $f_{\text{obs}}-M_*$ plane

In Figure 7 (right), we found a large spread in the $f_{\text{obs}}-M_*$ relation across galaxies in our sample. As more than 30% of the galaxies deviate from the average relationship derived from the stacking analysis, even when considering 1σ errors, the variance is not likely to come from the measurement errors. Such a variation has been reported in ALMA observations toward UV-bright galaxies at $z > 4$ (Fudamoto et al. 2020a; Inami et al. 2022). They investigated the relationship between UV continuum slope (β_{UV}) and IRX. Previous studies predict that the scatter could be caused by dust grain type (e.g., Ferrara et al. 2017), dust geometry (e.g., Witt & Gordon 2000), stellar populations (e.g., Popping et al. 2017a), stellar or dust assembly (e.g., Popping et al. 2017b), spatial decoupling of UV and IR emission due to galactic interaction or dust-enshrouded nuclear starbursts (e.g., Howell et al. 2010), and inclination (e.g., Wang et al. 2018). As it is

Table 1. Dust continuum properties of the CRISTAL galaxies

ID	$\log_{10} M_*$ [M_\odot]	S/N	S_{uv}^a [mJy]	S_{tap}^b [mJy]	$\log_{10} L_{\text{IR}}$ [L_\odot]	f_{obs}	$r_{e,\text{dust}}$ [arcsec]	$r_{e,\text{UV}}^c$ [arcsec]	class ^d
CRISTAL main sample									
CRISTAL-01a	10.65 ± 0.50	-	-	≤ 0.251	≤ 11.54	≤ 0.426	-	0.154 ± 0.007	multiple
CRISTAL-02	10.30 ± 0.28	9.3	0.405 ± 0.075	0.362 ± 0.055	11.80 ^{+0.06} _{-0.07}	0.629 ^{+0.105} _{-0.122}	0.326 ± 0.076	- ^e	multiple
CRISTAL-03	10.40 ± 0.29	4.8	0.044 ± 0.014	0.037 ± 0.016	10.86 ^{+0.16} _{-0.25}	0.210 ^{+0.077} _{-0.122}	≤ 0.369 ^f	0.173 ± 0.007	single
CRISTAL-04a	10.15 ± 0.29	7.6	0.174 ± 0.043	0.164 ± 0.035	11.36 ^{+0.08} _{-0.10}	0.587 ^{+0.130} _{-0.162}	0.130 ± 0.072	0.154 ± 0.007	multiple
CRISTAL-05	10.16 ± 0.35	6.7	0.141 ± 0.044	0.122 ± 0.026	11.36 ^{+0.08} _{-0.11}	0.574 ^{+0.129} _{-0.161}	0.244 ± 0.105	0.061 ± 0.003	single
CRISTAL-06a	10.09 ± 0.30	13.1	0.280 ± 0.051	0.254 ± 0.029	11.55 ^{+0.05} _{-0.05}	0.794 ^{+0.109} _{-0.122}	0.310 ± 0.071	0.214 ± 0.010	multiple
CRISTAL-07ab	10.00 ± 0.33	4.5	0.078 ± 0.037	0.085 ± 0.019	11.16 ^{+0.09} _{-0.11}	0.331 ^{+0.071} _{-0.089}	0.201 ± 0.153	0.146 ± 0.008	multiple
CRISTAL-08	9.85 ± 0.36	-	-	≤ 0.073	≤ 10.99	≤ 0.363	-	0.380 ± 0.012	single
CRISTAL-09	9.84 ± 0.39	4.5	0.083 ± 0.032	0.080 ± 0.036	11.18 ^{+0.16} _{-0.26}	0.463 ^{+0.189} _{-0.302}	0.104 ± 0.079	0.028 ± 0.002	single
CRISTAL-10	9.99 ± 0.31	4.4	0.122 ± 0.058	0.101 ± 0.026	11.29 ^{+0.1} _{-0.13}	0.333 ^{+0.08} _{-0.104}	0.405 ± 0.226	- ^e	multiple
CRISTAL-11a	9.68 ± 0.33	4.6	0.137 ± 0.055	0.095 ± 0.051	11.11 ^{+0.19} _{-0.33}	0.542 ^{+0.265} _{-0.475}	0.116 ± 0.091	0.066 ± 0.004	single
CRISTAL-12	9.30 ± 0.47	-	-	≤ 0.029	≤ 10.73	≤ 0.535	-	- ^g	single
CRISTAL-13	9.65 ± 0.34	6.6	0.137 ± 0.039	0.120 ± 0.037	11.23 ^{+0.12} _{-0.16}	0.621 ^{+0.196} _{-0.268}	0.092 ± 0.070	0.056 ± 0.023	multiple
CRISTAL-14	9.53 ± 0.38	-	-	≤ 0.044	≤ 10.77	≤ 0.364	-	0.054 ± 0.011	single
CRISTAL-15	9.69 ± 0.33	-	-	≤ 0.046	≤ 10.81	≤ 0.275	-	- ^e	single
CRISTAL-16	9.60 ± 0.39	-	-	≤ 0.037	≤ 10.85	≤ 0.386	-	0.250 ± 0.020	single
CRISTAL-17	9.51 ± 0.40	-	-	≤ 0.035	≤ 10.83	≤ 0.362	-	- ^g	single
CRISTAL-19	9.51 ± 0.36	5.5	0.093 ± 0.038	0.078 ± 0.022	11.13 ^{+0.11} _{-0.15}	0.572 ^{+0.165} _{-0.220}	0.262 ± 0.153	0.097 ± 0.009	single
CRISTAL+ sample									
CRISTAL-20	10.11 ± 0.35	13.8	0.157 ± 0.025	0.144 ± 0.015	11.43 ^{+0.04} _{-0.05}	0.459 ^{+0.049} _{-0.055}	0.251 ± 0.054	0.060 ± 0.002	single
CRISTAL-21	10.11 ± 0.32	4.9	0.528 ± 0.219	0.201 ± 0.046	11.54 ^{+0.09} _{-0.11}	0.613 ^{+0.148} _{-0.187}	1.160 ± 0.499	0.062 ± 0.003	single
CRISTAL-22ab ^h	10.35 ± 0.37	22.9	1.522 ± 0.074	1.343 ± 0.158	12.42 ^{+0.05} _{-0.05}	0.927 ^{+0.140} _{-0.158}	0.150 ± 0.011	0.129 ± 0.008	multiple
CRISTAL-23a	10.55 ± 0.29	12.2	1.142 ± 0.211	0.831 ± 0.087	12.07 ^{+0.04} _{-0.05}	0.847 ^{+0.111} _{-0.123}	0.486 ± 0.093	0.091 ± 0.006	multiple
CRISTAL-24	10.53 ± 0.08	22.3	1.201 ± 0.100	1.236 ± 0.092	12.24 ^{+0.03} _{-0.03}	0.956 ^{+0.094} _{-0.102}	0.204 ± 0.028	0.105 ± 0.020	single
CRISTAL-25	10.90 ± 0.32	7.8	0.501 ± 0.137	0.402 ± 0.065	11.75 ^{+0.06} _{-0.08}	0.681 ^{+0.123} _{-0.145}	0.320 ± 0.116	0.131 ± 0.004	single
serendipitously detected sources									
CRISTAL-01b	9.81 ± 0.34	4.4	0.449 ± 0.165	0.340 ± 0.066	11.67 ^{+0.08} _{-0.09}	0.715 ^{+0.156} _{-0.190}	0.331 ± 0.153	0.095 ± 0.005	multiple
CRISTAL-07c	10.21 ± 0.35	7.0	0.160 ± 0.045	0.123 ± 0.024	11.32 ^{+0.08} _{-0.09}	0.683 ^{+0.148} _{-0.181}	0.139 ± 0.077	0.143 ± 0.015	single

Notes. ^(a) rest frame 158 μm fluxes measured with UVMULTIFIT. ^(b) rest frame 158 μm fluxes measured with tapered images (see Section 3.2). 4- σ upper limits are shown if source S/N < 4. ^(c) circularized *HST*/F160W size with fixing sersic index to unity. ^(d) classification based on the *HST*/F160W image. ^(e) galfit does not converge due to the existence of multiple sources having similar brightness. ^(f) 1- σ upper limit of the size. ^(g) no clear counterpart or low S/N in *HST*/F160W image. ^(h) S_{uv} indicate total flux of main+sub components, and $r_{e,\text{dust}}/r_{e,\text{UV}}$ are the effective radius of the main component (See Figure 2).

difficult to demonstrate the dependence of dust/stellar properties such as grain type, geometry, or assembly based on our ALMA observations, we discuss the potential correlation between f_{obs} and morphology. We note that no correlation is identified between f_{obs} and the stellar ages derived from SED fitting obtained in Section 2.2.

4.2.1. inhomogeneous dust reddening

The first possible explanation for the variation in the obscured fraction is inhomogeneous dust reddening, such as a global spatial offset between dust-enshrouded and dust-free star-forming regions. Recently, Bowler et al. (2022) discussed the impact of the spatial distribution of rest-UV and IR emission on the UV-IR energy balance at $z \sim 7$ (see also Inami et al. 2022). They found a correlation between a redder UV slope and a peak of FIR emission detected in ALMA and suggest that inhomogeneous dust reddening might be responsible for variations in

the spatially-integrated IRX- β_{UV} relation (see also, Vallini et al. 2015; Behrens et al. 2018).

In Figure 8, we show the distance from our best-fit $f_{\text{obs}}-M_*$ relation (Δf_{obs}) as a function of the spatial offset of the central position between the UV and dust continuum. We find a negative correlation between Δf_{obs} and the spatial offset within 1 σ uncertainty of the correlation coefficient of $\rho_{\text{corr}} = -0.58^{+0.30}_{-0.20}$ with a p -value of 0.082. This correlation suggests that the decoupling of UV and IR emissions contributes to the escape of UV photons from interstellar space, and makes the variation on the obscured fraction.

What causes the spatial offset between UV- and IR-bright star-forming regions? Numerical simulations incorporating radiative transfer suggest that galactic interaction or feedback are possible mechanisms to decouple UV- and IR-bright regions (e.g., Yajima et al. 2011; Safarzadeh et al. 2017; Arata et al. 2019; Liang et al. 2021). For the feedback case, it is expected that galaxies with higher sSFR will tend to show larger peak offsets because star formation-driven outflows are more prevalent (e.g.,

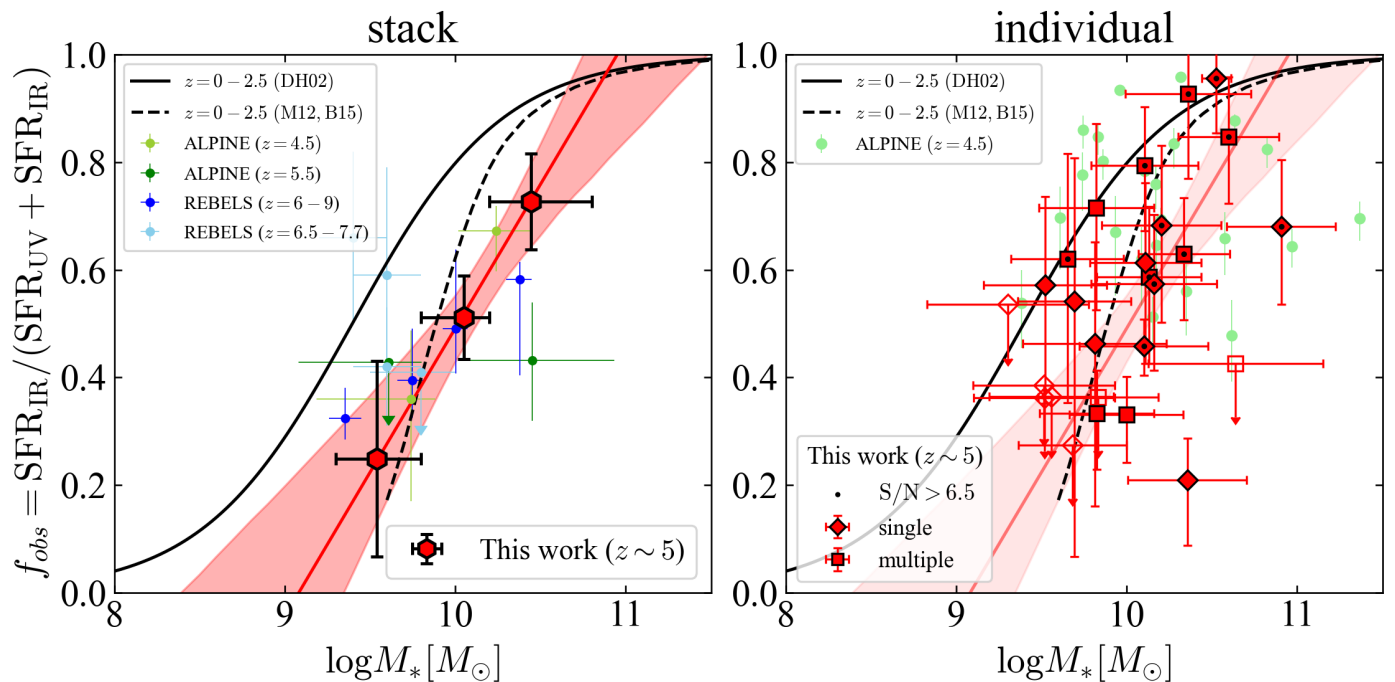


Fig. 7. (left) The relationship between the obscured fraction and the stellar mass from stacking analysis. Black solid and dashed lines show the results from Whitaker et al. (2017) with two different dust emission templates of Dale & Helou (2002) template (D02) and Magdis et al. (2012) and Béthermin et al. (2015) template (M12, B15). The obscured fraction increases as a function of the stellar mass, and the trend has a good agreement with the results at $z \sim 5$ from the ALPINE survey (Fudamoto et al. 2020a) and those at $z \sim 6-9$ from the REBELS survey (Algera et al. 2023), while another result at $z \sim 6.5-7.7$ from the REBELS survey (Bowler et al. 2023) show an opposite trend with slightly higher f_{obs} at $M_* < 10^{10} M_\odot$. **(right)** The obscured fraction of the individual galaxies as a function of the stellar masses. The diamonds and squares correspond to the two classifications of single and multiple. We also show the results of the galaxies detected in the dust continuum at $z \sim 5$ (Fudamoto et al. 2020a). Our observations capture the galaxies with smaller f_{obs} compared with previous $z \sim 5$ galaxies individually detected thanks to deep observations. There is a significant variation in $f_{obs}-M_*$ relation from galaxy to galaxy.

Fujimoto et al. 2020; Faisst et al. 2020b). We divide the sample into two groups within $s\text{SFR} < 4 \text{ Gyr}^{-1}$ and $s\text{SFR} > 4 \text{ Gyr}^{-1}$ based on the total (IR+UV) SFR and compare the peak offset between UV and IR. There is no clear difference in the peak offset between the two groups, $0.150 \pm 0.046''$ for the galaxies within $s\text{SFR} < 4 \text{ Gyr}^{-1}$ and $0.150 \pm 0.038''$ for $s\text{SFR} > 4 \text{ Gyr}^{-1}$.

For the merger case, we expect a larger spatial offset in the “multiple” sample than the “single” sample because the galaxies classified as “multiple” correspond to a kind of early-stage merger. However, the peak offset between UV and IR does not exhibit a systematic offset between “multiple” ($0.145 \pm 0.048''$) and “single” ($0.155 \pm 0.041''$). Therefore the interaction is not likely to primary cause of the decoupling. While the merger activity does not generate the decoupling of the dust-obscured and unobscured star-forming regions, it may accelerate the obscured star formation. In Figure 7, we plot our result separately for single (isolated) and multiple (merging) galaxies. Most highly obscured galaxies tend to have high total SFRs and show merging signatures in *HST* images. Also, The average obscured fraction and SFR of the multiple galaxy sample ($\langle f_{obs} \rangle_{\text{multiple}} = 0.43^{+0.03}_{-0.03}$, $\langle \log_{10} \text{SFR} [M_\odot \text{ yr}^{-1}] \rangle_{\text{multiple}} = 1.97^{+0.60}_{-0.54}$) is higher than that of the single galaxy samples ($\langle f_{obs} \rangle_{\text{single}} = 0.34^{+0.03}_{-0.03}$, $\langle \log_{10} \text{SFR} [M_\odot \text{ yr}^{-1}] \rangle_{\text{single}} = 1.58^{+0.10}_{-0.11}$). Our results suggest that galaxy interactions may boost not only the star formation activities but also the obscured fraction within almost the same stellar mass range, and the mixture of the different merger stages and isolated disks leads to the variety in $f_{obs}-M_*$ plane.

Another potential physical reason for the displacement is a multiphase structure of the ISM, for which one-zone ISM models assumed in the IRX- β (or $f_{obs}-M_*$) relation cannot be applied. As discussed in Ferrara et al. (2022), molecular index

$I_m (= F_{158}/F_{1500}/(\beta - \beta_{\text{int}}))$ might represent a good indicator of such a multi-phase ISM structure. We test the hypothesis by comparing the UV-dust spatial offset and I_m under the assumption of $\beta_{\text{int}} = -2.41$ following Inami et al. (2022), but we do not find a clear correlation between them ($\rho_{\text{corr}} = -0.218^{+0.262}_{-0.234}$ with a p -value of 0.401). This result is mainly due to the small measured values of the UV-dust offset compared to Inami et al. (2022). Interestingly, though, CRISTAL-24 shows a very high I_m of ~ 5000 with a relatively blue UV slope $\beta = -1.55$. An inconsistent SFR_{SED} and $\text{SFR}_{\text{UV+IR}}$ in CRISTAL-24 described in Section 2.2 may indicate multi-phase and component nature of the CRISTAL-24.

4.2.2. concentration of the star-forming regions

Since we do not find clear dependence on the potential interactions or UV-dust offsets, we will now compare f_{obs} with the compactness of the star-forming regions. Whitaker et al. (2017) indicate that the spatial extent of the star-forming region affects the obscured fraction (see also, Smail et al. 2021). Howell et al. (2010) mention that dust-enshrouded central starburst may lead to a diversity of the obscured fraction. We derive the compactness of the dust-obscured star-forming region as Σ_{IR} computed from infrared luminosities and effective radii of the dust continuum. We also check the dependence of Δf_{obs} on the size ratio between UV and dust emission ($r_{e,\text{dust}}/r_{e,\text{UV}}$). We find that there is no clear correlation between Δf_{obs} and the size ratio ($\rho_{\text{corr}} = 0.11^{+0.28}_{-0.27}$ with a p -value of 0.693 respectively) but Σ_{IR} has potential correlation with f_{obs} ($\rho_{\text{corr}} = 0.30^{+0.22}_{-0.26}$ with a p -value of 0.245). Enhancement of the dust-obscured star formation activity could relate to the concentration of the young, active dust-

enshrouded star formation regions, which may be accelerated by unstable disks with high gas mass fraction (Dekel et al. 2009; Tacconi et al. 2013; Scoville et al. 2017; Dessauges-Zavadsky et al. 2020). Since starbursts induced by the galaxy interaction could concentrate the gas and dust into the central parts of galaxies (e.g., Barnes & Hernquist 1996), it may accelerate the dust obscuration of the galaxy and could explain the positive trend between the obscured fraction and Σ_{IR} or merging signatures.

4.2.3. inclination

Both observations (e.g., Leslie et al. 2018) and simulations (e.g., Jonsson et al. 2010) studies suggest that an apparent UV-IR energy balance can be affected by a viewing angle of disk galaxies i.e., inclination. There is a systematic offset of ~ 0.5 dex in IRX values between edge-on and face-on galaxies (Wang et al. 2018). While the inclinations are calculated from the axis ratios, the axis ratios of the UV continua may not be a proper indicator of an inclination due to severe dust attenuation. We do not find a correlation between the axis ratio of the UV continuum and Δf_{obs} ($\rho_{\text{corr}} = -0.09^{+0.28}_{-0.27}$ with a p -value of 0.761). Moreover, only a few CRISTAL galaxies have constraints on the axis ratios in dust emission. The current data quality is not sufficient to discuss the possibility that inclinations explain the variation in f_{obs} . It is worth noting that two galaxies with relatively large f_{obs} (> 0.7) have axis ratios of $\sim 0.2 - 0.3$ in the dust emission, suggesting that an edge-on view of disk galaxies may make the obscured fraction higher. Also, note that the axis ratio of [CII] emission also possibly correlates with Δf_{obs} with $\rho_{\text{corr}} = -0.35^{+0.27}_{-0.22}$ and a p -value of 0.203, where the axis ratio of [CII] is measured with the similar way as this work (Ikeda et al. in prep). Future *JWST* observations will unveil rest-frame optical light distribution, which traces stellar mass distributions. It will allow us to investigate the inclination dependence of f_{obs} toward high redshift galaxies (e.g., Cochrane et al. 2023).

4.2.4. Caveat

One caveat of our analysis is that we use the single template of FIR SEDs for all CRISTAL galaxies. Therefore we do not take into account variation of T_{dust} or β_{dust} characterizing FIR SEDs. If actual T_{dust} of the galaxies having low (high) f_{obs} are larger (smaller) than that of the FIR SED used in this work ($T_{\text{dust}} \sim 40\text{K}$, see Béthermin et al. 2020), the spread of f_{obs} becomes smaller. A variation of $T_d \sim 20\text{K}$ changes infrared luminosities with $\Delta L_{\text{IR}} \sim 0.25$ dex and the obscured fractions with $\Delta f_{\text{obs}} \sim 0.15$. Since we find a potential correlation between Σ_{IR} and f_{obs} , the galaxies with high (low) f_{obs} can have higher (lower) T_{dust} or L_{IR} than the current estimation if we assume there is a positive correlation between Σ_{IR} and T_{dust} revealed in previous results (e.g., Díaz-Santos et al. 2017; Dudzevičiūtė et al. 2020). In this case, the range of variation expands beyond the current estimation. We need high-frequency ALMA bands (Band-8/9/10), which cover the frequencies corresponding to the peak of the dust continuum emission, to derive the FIR SEDs of individual galaxies. While high-frequency band observations towards large galaxy samples are still challenging due to limitations such as sensitivities or atmospheric conditions, case studies of some representative galaxies will help us to know accurate FIR SED.

4.3. Star formation mode of $z \sim 5$ LBGs

4.3.1. Extended dust-obscured star formation

As described in Section 3.4 and Figure 6, we find $r_{e,\text{dust}}$ are comparable or slightly larger than $r_{e,\text{UV}}$. Our size ratios are not consistent with the results from TNG50 simulation expecting $r_{e,\text{UV}}/r_{e,\text{dust}} \sim 2-4$ in the stellar mass range of the CRISTAL

galaxies (Popping et al. 2022). As Popping et al. (2022) measure half-light radii of UV and dust continuum at the almost same observed wavelength with our observations ($\lambda_{\text{obs}} = 1.6\mu\text{m}$ and $850\mu\text{m}$ for UV and dust continuum, respectively), the size ratios can be directly compared.

Before comparing observational results and the simulation, we need to be careful about observational biases coming from the limited S/Ns or spatial resolutions. One possible reason for the extended dust continua is the source blending of nearby companions. To demonstrate how the companions affect the size measurement, we re-run GALFIT to the *HST* images after matching *HST* PSF to ALMA beam size with PHOTUTILS/PSF and adding white noises to match peak S/Ns of UV continuum to dust continuum. As ALMA beam sizes can be changed by different weighting of visibilities, here we use natural-weighted beam sizes of each visibilities as nominal target beam sizes of the PSF matching. Typically the naturally-weighted ALMA beam sizes ($0.46'' = 2.9\text{kpc}$ at $z = 5$) are larger than *HST* PSFs ($0.20'' = 1.3\text{kpc}$ at $z = 5$). We test the procedure in three CRISTAL galaxies (CRISTAL-02, 06a, and 22ab) since (i) they have nearby companions in *HST* images and (ii) their dust continua are detected in $S/N > 6.5$. The results reveal the measured sizes are consistent with those without PSF and S/N matching. Therefore source blending is not enough to explain the extended dust continua in CRISTAL galaxies. Another possible reason is the limited S/N, but it is not likely to be a possible reason because $r_{e,\text{dust}}$ are still only slightly larger than $r_{e,\text{UV}}$ when we only take the sources with $S/N > 6.5$ into account.

In Figure 9, we show the stacked radial profile of the dust and UV continuum to obtain better S/N than the individual measurements. Here we stacked UV and dust continua of single (“isolated”) galaxy samples to avoid blending with companions. We follow the visibility-based method described in Section C.2 regarding the stacking of ALMA data. About the stacked UV continuum image, we shift the fitting center to the central coordinate of the image and match the PSFs of each *HST* image to that of the stacked ALMA image, and then take an average. Again, the stacked radial profile shows that the spatial extent of the dust continuum is slightly more extended than that of the UV continuum.

Therefore, the spatially extended dust continuum does not originate from the observation, but from the properties of the galaxy itself. Possible physical interpretations of $r_{e,\text{UV}}/r_{e,\text{dust}} \lesssim 1$ are clumpy gas distributions that enable UV photons to radiate molecular clouds out to the outskirts of the galaxies, even though these clouds are slightly distant from young massive stars. The theoretical and observational studies suggest an increase of clumpy star-forming galaxies at high redshift (e.g., Genzel et al. 2008; Dekel et al. 2009; Tadaki et al. 2014; Guo et al. 2015). In this case, the dust temperature is expected to decrease from the center to the outskirts of the galaxy. In our conversion from $S_{158\mu\text{m}}$ to L_{IR} , if the dust temperature has a negative gradient of $\Delta T_{\text{dust}} \sim 10\text{K}$ from center to the outskirts (e.g., Arata et al. 2019), the infrared luminosity decrease ~ 0.3 dex, and the actual spatial extent of the dust-obscured star-forming region becomes comparable with that of the dust-unobscured ones as predicted in SERRA simulation (e.g., Pallottini et al. 2022). Another possibility is that rest-UV observations do not trace global star formation activities but massive star-forming clumps within the galaxies.

4.3.2. Stellar mass-size relation

Several *HST*-based studies of galaxy morphology reveal that the size of the stellar distribution depends on both redshift and stellar mass (e.g., van der Wel et al. 2014; Shibuya et al. 2016). The stellar sizes become smaller with increasing redshift at fixed stellar mass and with decreasing stellar mass at fixed redshift. Fujimoto et al. (2017) suggest dust continuum sizes also follow a similar

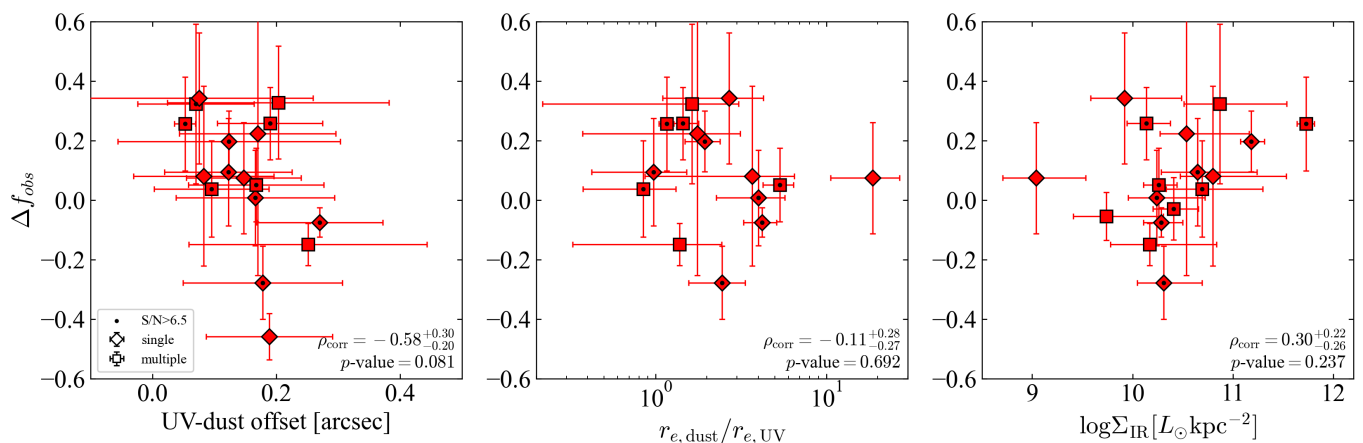


Fig. 8. The distance from an average $f_{\text{obs}}-M_*$ relation as a function of (left) the spatial offset of the central position between UV and dust emission, (middle) the size ratio between UV and dust emission, and (right) the surface density of L_{IR} . Galaxies without clear main UV components and without dust continuum detection at $< 4\sigma$ are not shown. Based on the Spearman correlation coefficients and p -values, f_{obs} has a correlation with the UV-dust spatial offset and Σ_{IR} . On the other hand, there is no correlation between f_{obs} and the size ratio between UV and dust emission.

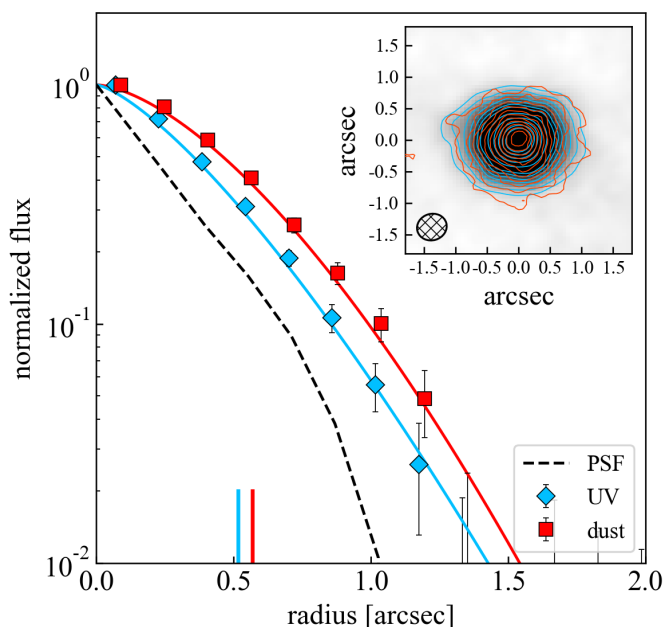


Fig. 9. Normalized radial profiles of the stacked dust and UV continua (red and blue respectively). The perpendicular lines are effective radii derived from the best-fit Sérsic profile in the corresponding colors. Here we stack only single (“isolated”) galaxy samples to avoid the blending of the companion. The matched PSF size is also shown in a black solid line. The inset shows the 2D distributions. The spatial extent of the dust continuum is more extended to that of the UV continuum.

evolutionary trend with redshift and stellar mass. Because the dust continuum traces recent star formation events and the stellar emission traces histories of the star formation in the galaxies, the size comparison of the dust continuum and stellar continuum at similar epochs brings a crucial perspective on the morphological transformation of galaxies.

In Figure 10, we plot rest-frame $158\mu\text{m}$ dust continuum sizes of the CRISTAL galaxies as a function of their stellar masses. We also show typical rest-frame optical sizes of late-type galaxies (LTGs) and early-type galaxies (ETGs) (van der Wel et al. 2014) and rest-frame UV sizes (Shibuya et al. 2016) of Lyman-break galaxies (LBGs) as a function of stellar masses at $z \sim 5$. Note that we extrapolated the redshift evolution reported in van der

Wel et al. (2014) to $z \sim 5$ because the rest-frame wavelength of 5000 \AA used to measure stellar sizes in van der Wel et al. (2014) redshifted to the outside of the coverage of *HST* NIR filters. Therefore we also show recent *JWST* studies of the rest-frame UV sizes of LBGs (Morishita et al. 2023, see also Ono et al. 2023), and those of the rest-frame optical sizes of LTGs (Ward et al. 2023) and ETGs (Ito et al. 2023). The extrapolated van der Wel et al. (2014) relation might be slightly overestimated, although the difference does not impact our conclusion. Future direct comparison with the rest-frame optical sizes measured by *JWST* observations will allow us to capture the dust, UV, and stellar size properties of the typical galaxies individually.

The dust continuum sizes and stellar masses of more dusty galaxies follow the trend of ETGs (e.g., Gómez-Guijarro et al. 2022). These results imply that massive dusty galaxies are in a build-up phase of central stellar cores (i.e., stellar bulge) of massive elliptical galaxies (e.g., Toft et al. 2014; Gómez-Guijarro et al. 2022) or evolve into compact quiescent galaxies (e.g., Toft et al. 2014; Ikarashi et al. 2015; Barro et al. 2016). This is consistent with the studies that investigated the stellar and dust continuum sizes of individual galaxies at $z \sim 2-3$ (Simpson et al. 2015; Gullberg et al. 2019; Lang et al. 2019; Tadaki et al. 2020a). In contrast, as shown in Figure 10, the dust continuum sizes of CRISTAL galaxies follow a similar trend as the mass-size relation of LTGs or LBGs. Average stellar mass ($M_* \sim 10^{9.8} M_\odot$) and effective radius ($\sim 1.7 \text{ kpc}$) are in excellent agreement with them on the mass-size plane. Our result suggests that typical star-forming galaxies with $M_* \sim 10^{10} M_\odot$ might be still growing their disks via global star formation.

4.4. Morphological transformation and descendant

Recent wide field surveys revealed typical dark matter halo masses of the bright LBGs ($M_{\text{UV}} \sim -21 \text{ mag}$, $M_* \sim 10^{10} M_\odot$ in stellar mass) at $z = 4-6$ are $M_{\text{halo}} \sim 10^{12} M_\odot$ (e.g., Harikane et al. 2018). If we assume the median growth rate for their dark matter haloes from N-body simulations, dark matter haloes with masses of $M_{\text{halo}} \sim 10^{12} M_\odot$ at $z \sim 5$ evolve into haloes with $M_{\text{halo}} \sim 10^{12.5-13.0} M_\odot$ at $z \sim 2$, which host massive galaxies with mass of $M_* \sim 10^{11} M_\odot$ at $z \sim 2$. In the case that the bright LBGs at $z = 4-6$ continue to stay MS to $z = 2$, their stellar masses could be $M_* \gtrsim 10^{11} M_\odot$. From these estimation, the bright LBGs with $M_* \sim 10^{10} M_\odot$ at $z = 4-6$ are likely to evolve into $z \sim 2$ massive galaxies with $M_* \sim 10^{11} M_\odot$.

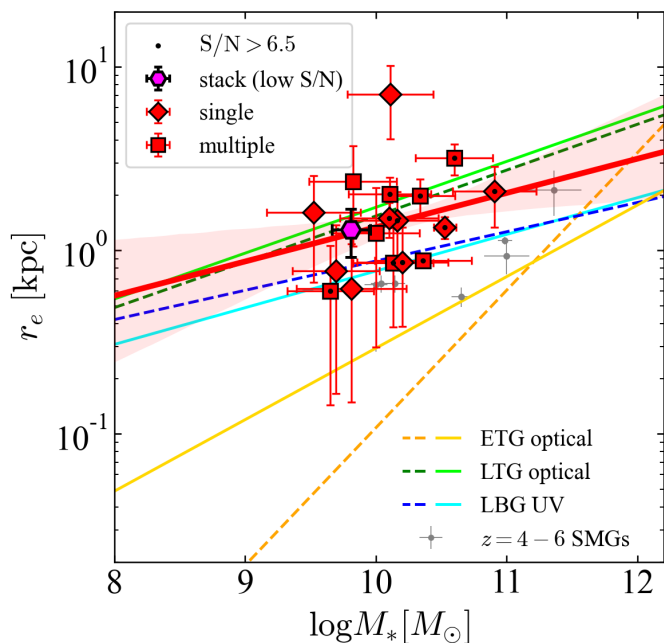


Fig. 10. Stellar mass versus effective radii of the dust continuum for the CRISTAL galaxies. The dashed and solid lines show the scaling relations derived with *HST* and *JWST*. The orange and green colors represent the rest-frame optical sizes of ETGs (van der Wel et al. 2014; Ito et al. 2023), and the LTGs (van der Wel et al. 2014; Ward et al. 2023). The blue colors indicate rest-frame UV sizes of LBGs (Shibuya et al. 2016; Morishita et al. 2023). The average stellar mass and stacked size derived in Section C.2 is also shown. CRISTAL galaxies are distributed around the scaling sequence of LTGs or LBGs in contrast to the massive SMGs that show consistent dust continuum sizes and stellar masses with those of ETGs (Riechers et al. 2014; De Breuck et al. 2014; Hodge et al. 2015; Gómez-Guijarro et al. 2018; Casey et al. 2019; Tadaki et al. 2020b).

As the average structural evolutions of SFGs are expected to follow the scaling relation on the mass-size plane, a bright LBG at $z = 4-6$ will grow its stellar disk by a factor of two after a ten-fold increase in stellar mass. The expected size of the stellar disks is consistent with that of massive DSFGs at $z \sim 2$. This consistency also supports that the bright LBGs at $z = 4-6$ are expanding their stellar disks through widespread star formation.

5. Summary and Conclusion

In this paper, we have focused on the dust continuum emissions of $z \sim 5$ normal star-forming galaxies as a part of the ALMA cycle-8 large program, CRISTAL. We have examined the spatial extent of the dust-obscured and unobscured star formation, obscured fraction of star formation as a function of stellar mass ($f_{\text{obs}} - M_*$), and origin of the observed variation in f_{obs} with stellar mass on $f_{\text{obs}} - M_*$. The sample is representative of typical star-forming galaxies at $z = 4-6$ as almost all of them lie within 0.3 dex of the main sequence of star-forming galaxies in that redshift range. The stellar mass (M_*) and SFR of the target galaxies are the range of $\log_{10} M_* [M_{\odot}] \sim 9.5-11.0$ and $\log_{10} \text{SFR} [M_{\odot} \text{yr}^{-1}] \sim 1.0-2.7$. From individual measurements and stacking analysis, we found:

1. The CRISTAL galaxies have ~ 1 dex smaller infrared luminosities (L_{IR}) and are slightly more extended in dust continuum emission than DSFGs or SMGs. Consequently the median IR surface densities Σ_{IR} are ~ 10 times smaller (Figure 5). This suggests that representative galaxy population

at $z \sim 4-6$ undergoes moderate star formation with a lower Σ_{IR} compared with the dusty galaxies indicating intensive, centrally concentrated star formation.

2. The obscured fraction has a positive correlation with the stellar mass (Figure 7, left). Our averaged relationship is consistent with the previous results at $z \sim 5-9$ and supports that the obscured fraction at the range of $M_* < 10^{10} M_{\odot}$ does not show clear evolution from $z = 0-2.5$, but may decrease at the range of $M_* > 10^{10} M_{\odot}$. The possible evolution at the range of $M_* > 10^{10} M_{\odot}$ suggests the evolution of dust content from $z \sim 5$ to $z \sim 0-2.5$.
3. A large variation in $f_{\text{obs}} - M_*$ relation across galaxies in our sample. Through deep observations in our survey, we trace the galaxy with an obscured fraction of as low as 20%, which is smaller than what has been reported in previous surveys. We find a weak correlation between f_{obs} and potential merger identified by multiplicity, and compactness of the dust-obscured star-forming regions, but do not detect a correlation with the spatial offset between UV and dust continuum, or viewing angle (Figure 8). Some mechanisms such as interactions or rich gas accretions may enhance the concentration of gas and dust, and accelerate the obscuration of the star formation activities.
4. The effective radii of the dust continuum ($r_{e,\text{dust}}$) are comparable or ~ 2 times larger than that of the UV continuum ($r_{e,\text{UV}}$) in the individual comparison whereas the dust emission originates the dust heated by UV radiation from massive O/B type stars. These results are not consistent with the Illustris TNG50 simulation which expects $r_{e,\text{dust}}/r_{e,\text{UV}} \sim 0.25-0.5$ in the stellar mass range of the CRISTAL galaxies. With careful treatment and stacking analysis, we confirm comparable sizes of the dust and UV continuum do not come from observational uncertainties. The extended dust size may be due to (i) clumpy gas distribution makes UV photons possible to radiate molecular clouds around the outskirts of galaxies or (ii) rest-frame UV observations do not trace global star formation activities but massive star-forming clumps within galaxies.
5. The CRISTAL galaxies follow a similar trend as LTGs or LBGs in the stellar mass-size plane (Figure 10). They are distributed in a different regime compared with more dusty galaxies that follow the trend of ETGs. Our result suggests typical star-forming galaxies with $M_* \sim 10^{10} M_{\odot}$ are in a growing-up phase of disks through global star formation.
6. An expansion of the disks in $z \sim 5$ normal SFGs along with the star-forming sequence in the mass-size plane are completely consistent with the large stellar disks of massive galaxies at $z \sim 2$. An expansion of the stellar disks from $z \sim 5$ to $z \sim 2$ and the subsequent compaction events naturally explain morphological transformation and are consistent with previous studies examining massive galaxies at $z \sim 2$.

Our results emphasize the importance of considering the spatial extent of both the dust-unobscured and obscured star formation activities are important when studying their morphological transformation, especially given more than $\sim 50\%$ of the star-formation activities is obscured by the dust at the stellar mass range of $M_* > 10^{10} M_{\odot}$. Since the spatial extent of the dust-obscured star formation is almost comparable with that of the dust-unobscured one, normal star-forming galaxies at $z \sim 5$ are not making their sizes compact, but expanding their stellar disks. Inner structures of the typical star-forming galaxies at $z \sim 5$, at the end of the epoch of reionization, is an important question to be addressed with future ALMA and *JWST* observations, which will provide the more secure spatial extent of dust-obscured star-forming regions or other components such as pre-existing stellar disks or ionized gas. Also, ALMA has the capability of high-frequency observations such as band-8/9/10, which enables us to constrain the FIR SED of each galaxy and bring us to a clearer picture of the obscured star formation.

Acknowledgements. This paper makes use of the following ALMA data: ADS/JAO.ALMA#2017.1.00428.S, #2018.1.01359.S, #2018.1.01605.S, #2019.1.01075.S, #2019.1.00226.S, and #2021.1.00280.L. ALMA is a partnership of ESO (representing its member states), NSF (USA), and NINS (Japan), together with NRC (Canada), MOST and ASIAA (Taiwan), and KASI (Republic of Korea), in cooperation with the Republic of Chile. The Joint ALMA Observatory is operated by ESO, AUI/NRAO, and NAOJ. This work was supported by JSPS KAKENHI grant No. 23K03466. I.M. is financially supported by Grants-in-Aid for Japan Society for the Promotion of Science (JSPS) Fellows (KAKENHI Number 22KJ0821). R.H.-C. thanks to the Max Planck Society for support under the Partner Group project "The Baryon Cycle in Galaxies" between the Max Planck for Extraterrestrial Physics and the Universidad de Concepción. R.H.-C. also gratefully acknowledges financial support from Millenium Nucleus NCN19058 (TITANs), and ANID BASAL projects ACE210002 and FB210003. M.A. acknowledges support from FONDECYT grant 1211951. M.A. and R.J.A. acknowledge support from ANID BASAL project grant FB210003. R.J.A. was supported by FONDECYT grant number 123171. R.B. acknowledges support from an STFC Ernest Rutherford Fellowship [grant number ST/T003596/1]. R.D. is supported by the Australian Research Council Centre of Excellence for All Sky Astrophysics in 3 Dimensions (ASTRO 3D), through project number CE170100013. A.F. acknowledges support from the ERC Advanced Grant INTERSTELLAR H2020/740120. T.N. acknowledges support from the Deutsche Forschungsgemeinschaft (DFG, German Research Foundation) under Germany's Excellence Strategy - EXC-2094 - 390783311 from the DFG Cluster of Excellence "ORIGINS". M.R. acknowledges support from project PID2020-114414GB-I00, financed by MCIN/AEI/10.13039/501100011033. H.Ü. gratefully acknowledges support by the Isaac Newton Trust and by the Kavli Foundation through a Newton-Kavli Junior Fellowship. Data analysis was in part carried out on the Multi-wavelength Data Analysis System operated by the Astronomy Data Center (ADC), National Astronomical Observatory of Japan.

Table A.1. Parameters for SED fitting

Parameters	Range
SFH: Delayed-τ (DELAYED)	
τ_{main} [Myr]	100, 300, 500, 1000, 2000, 5000
Age _{main} [Myr]	50 Myr steps in [50: 1000]
τ_{burst} [Myr]	10, 50, 100
Age _{burst} [Myr]	10, 20, 50
f_{burst} [Myr]	0.0, 0.05, 0.1, 0.2
SSP: BC03	
IMF	Chabrier
Z [Z_{\odot}]	0.2, 1
Nebular emission: CLOUDY	
$\log_{10} U$	-3.0
line width [km s^{-1}]	300
Dust attenuation: Calzetti00	
E(B-V)	0.1 steps in [0.0: 2.0]
E(B-V) factor	0.44
R_v	3.1

Appendix A: CIGALE parameters used to estimate global properties

We use all available broad- (BBs) and medium bands (MBs) in optical to near-infrared (NIR) for the SED fitting. In the COSMOS2015 catalog, we use 10 broad bands (u^* , B , V , r^+ , i^+ , z^{++} , Y , J , H , K_s) and 12 medium bands on Ground-based telescopes, and 4 *Spitzer* bands that achieve the best sensitivities among the bands covering similar wavelength. We take 4 broad bands (U , B , R , K_s) and 23 medium bands on Ground-based telescopes, and 10 *HST* and 4 *Spitzer* bands on space telescopes from the ASTRODEEP catalog. We extract the total fluxes of the counterparts of the CRISTAL galaxies from the corresponding catalogs. Table A.1 shows parameters used in SED fitting to derive stellar masses and SFRs (see Section 2.2).

Appendix B: comparison of SFR_{SED} and $\text{SFR}_{\text{UV}} + \text{SFR}_{\text{IR}}$

In Figure B.1, we compare $\text{SFR}_{\text{UV}} + \text{SFR}_{\text{IR}}$ and SFR_{SED} . $\text{SFR}_{\text{UV}} + \text{SFR}_{\text{IR}}$ is calculated by summing up SFR_{UV} from best-fit SED and SFR_{IR} from the rest-frame $158\mu\text{m}$ dust continuum flux and SFR_{SED} is computed by averaging the SFH over 100 Myr. SFR_{SED} is broadly consistent with $\text{SFR}_{\text{UV}} + \text{SFR}_{\text{IR}}$. CRISTAL-24 show ~ 1.4 dex smaller SFR_{SED} than $\text{SFR}_{\text{UV}} + \text{SFR}_{\text{IR}}$. This difference is due to the degeneracy of the dust extinction and stellar age and makes CRISTAL-24 distribute ~ 1.2 dex lower than the main sequence.

Appendix C: Validation of the dust size measurement

As shown in Table 1, about half of the CRISTAL galaxies range $4.4 < \text{S/N} < 5.5$ in the dust continuum images. These S/Ns might translate to significant uncertainties in our flux measurements but also to systematic errors in the sizes. To evaluate uncertainties of the size measurement through visibility fitting and confirm the validity of the size measurement, we conducted a Monte Carlo simulation and a stacking analysis toward fainter CRISTAL galaxies.

Appendix C.1: Monte-Carlo simulation

Because the measured sizes might be affected by noise fluctuations, we need to know the dependence of the size measurement uncertainties on the source S/N.

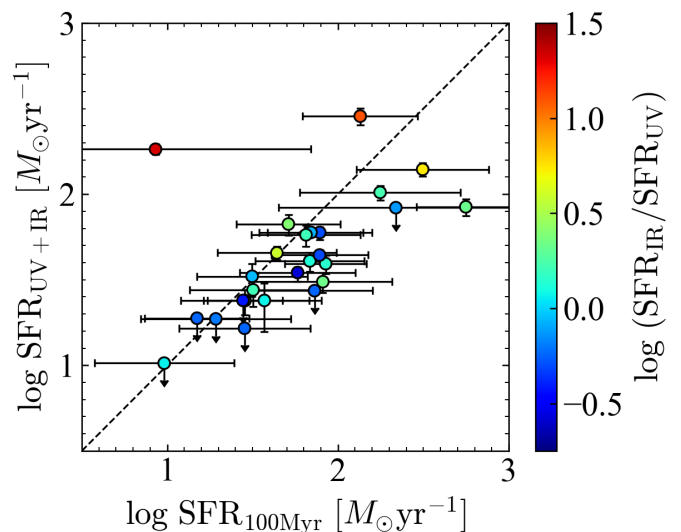


Fig. B.1. $\text{SFR}_{\text{UV}} + \text{SFR}_{\text{IR}}$ vs SFR_{SED} . The black dashed line represents a one-to-one relationship. SFR_{SED} is broadly consistent with $\text{SFR}_{\text{UV}} + \text{SFR}_{\text{IR}}$, except for CRISTAL-24.

In the following Monte-Carlo simulation, we use the visibilities of six galaxies (CRISTAL-01b, 07ab, 09, 10, 11a, and 19) that have relatively low S/Ns among the CRISTAL sample ($4.4 \leq \text{S/N} \leq 5.5$). This selection was made because galaxies with smaller S/N are anticipated to be more affected by noise fluctuations in size measurements. We take different array configurations used in each CRISTAL galaxy into account as the visibilities of the six galaxies encompass various representative uv coverages among those obtained in our observations. We create ~ 1500 (~ 300 in each field) artificial circular Gaussian sources with a log uniform distribution of total flux within a range of 0.025–1.25 mJy and effective radius ranging 0.025–1.5". After subtracting observed galaxies with the CASA task `TCLEAN`, we injected the generated mock sources in the visibilities at a random position and calculated source S/N in the same manner as referred to in Sec 3.1. When the mock source is detected at $4.4 < \text{S/N}$ (lowest S/N among observed galaxies in dust continuum), we fit a circular Gaussian model by setting an initial estimation of the central position to the artificial source center using `UVMULTIFIT`.

In Figure C.1, we plot the result of the Monte-Carlo simulation, with an average and standard deviation of the ratio between input and output values. As shown in Figure C.1, independent of the S/N of the source, we do not find any systematic offsets between intrinsic sizes and resulting measured sizes ($\text{size}_{\text{inp}}/\text{size}_{\text{fit}} \sim 0$). This result demonstrates the estimated sizes of these galaxies are on average reliable. However, careful treatment of individual sizes of the sources with $4.4 \leq \text{S/N} \leq 5.5$ is needed as the output sizes of these sources show large scatters from input sizes ($\text{size}_{\text{inp}}/\text{size}_{\text{fit}} = 0.07^{+0.67}_{-0.26}$) especially in the case that output sizes are less than 0.4" ($\text{size}_{\text{inp}}/\text{size}_{\text{fit}} = 0.09^{+0.83}_{-0.32}$). To obtain a better estimation of the size of these low-S/N sources, we additionally carry out a stacking analysis in the following section.

Appendix C.2: Stacked size

We now perform stacking analysis to check whether there are systematic biases in our size estimates. If galaxies included in stacking are intrinsically compact (extended) but appear as extended (compact) due to noise effects, stacked sizes are expected to become smaller (larger) than a weighted average of the indi-

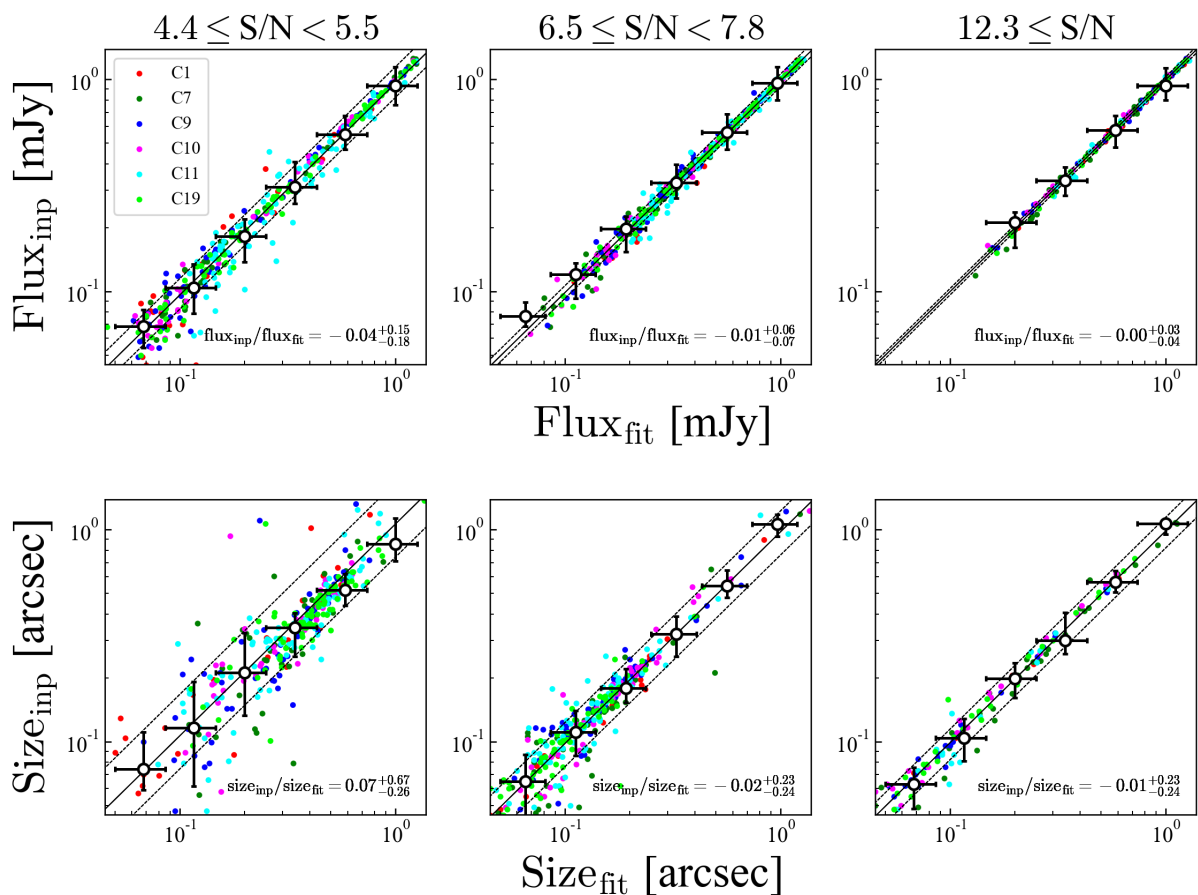


Fig. C.1. Comparison of the flux density and FWHM between fitting results and input models. The left, middle, and right panels show the results for sources detected at $S/N = 4.4-5.5$, $S/N = 6.5-7.8$ and $S/N \geq 12.3$, respectively. Different colors indicate different visibilities used in the simulation, corresponding to the different array configurations. White circles and error bars show $50 \pm 34\%$ percentiles in the bins of output values. Black solid and dashed lines correspond to the averages and standard deviations of the fitting results and output models, which are also shown in the bottom right of each panel.

vidual sizes. We perform the stacking analysis, especially for six of eight CRISTAL galaxies with $4.4 \leq S/N \leq 5.5$ (CRISTAL-01b, 07ab, 09, 10, 11a, and 19), to evaluate the potential size misestimations. We did not use the other two galaxies (CRISTAL-03 and 21) because CRISTAL-03 is not resolved and CRISTAL-21 has extremely extended sizes therefore they may affect stacked sizes strongly.

We align phase centers to the measured central position and set the phase center to a common coordinate of $\alpha = 00^{\text{h}} 00^{\text{m}} 00^{\text{s}}$; $\delta = 00^{\text{d}} 00^{\text{m}} 00^{\text{s}}$ (J2000) with CASA task `FIXPLANET`. We concatenate all visibilities into a single measurement set with the `CONCAT` task. Finally, we measured the sizes with `UVMULTIFIT`.

The estimated average size is $0.209 \pm 0.061''$, which is consistent with the average of the individually measured sizes ($0.237''$) within 1σ uncertainty. Therefore we conclude that the individual measurements of the six CRISTAL galaxies listed above are reliable. While the stacked measurements do not significantly affect the conclusion, we also plot the stacked size in Figure 10.

Appendix D: Sérsic index-dependence of the UV sizes

In Figure D.1, we compare the derived UV sizes under the assumption of Sérsic index $n = 1$ and $n = \text{free}$. Overall, there is no systematic difference between the two sizes. CRISTAL-25 shows a larger size in the case of $n = \text{free}$ because the best-fit

Sérsic index is larger than unity ($n = 7.3 \pm 1.7$). We note that this size difference of CRISTAL-25 does not affect the conclusion.

Appendix E: fitting results of ALMA and HST

Figure E.1 shows the results of the dust continuum size measurements in the visibility domain. The left and middle panels show the observed and residual images respectively. The observed and model images are natural-weighted in Figure E.1. The right panels show visibility amplitudes as a function of uv -distance from the central position of the fitting in two different binning scales (red and magenta). Red solid lines and shaded regions show best-fit models and uncertainties. To illustrate how the sizes are measured without the CRISTAL dataset, we add these results in gray points and solid lines. Figure E.3 shows results of the rest-frame UV size measurements in *HST*/F160W.

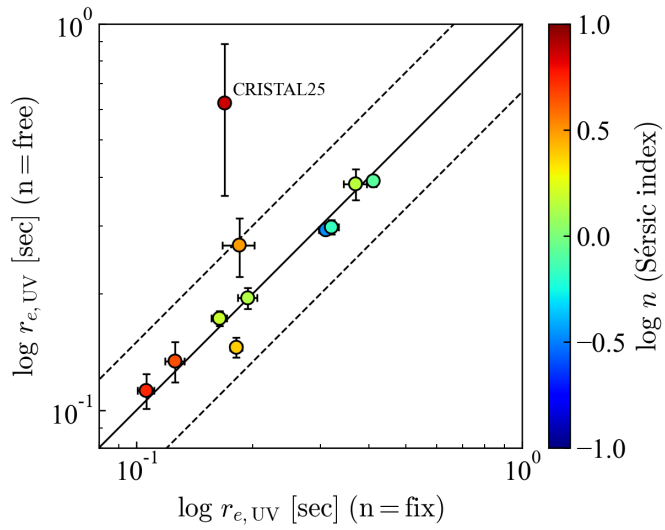


Fig. D.1. UV size comparison between the case with the Sérsic index fixed ($n = 1$) and with the Sérsic index free. Black solid and dashed lines indicate one-to-one relation and ± 0.3 dex. The sizes are almost consistent, except for CRISTAL-25 showing a large Sérsic index ($n = 7.3 \pm 1.7$).

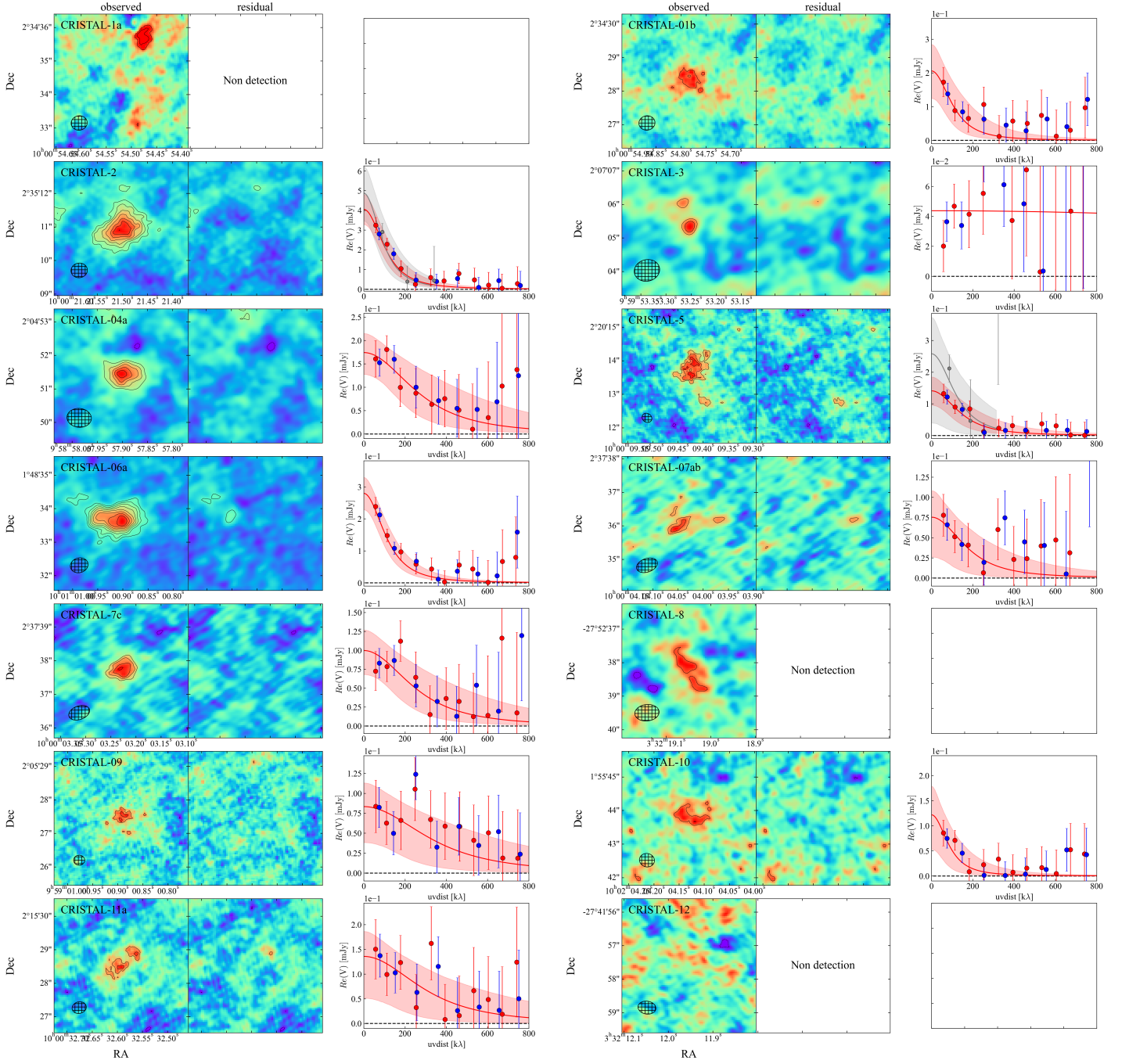


Fig. E.1. Fitting results of the ALMA images. The left and middle panels show the natural-weighted observed and residual images respectively. The contours indicate every 1σ from $\pm 3\sigma$ to 10σ and every 3σ from 10σ . The right panels show the visibility real part as a function of uv -distance from a central position of the fitting in two different binning scales (red and blue). Red solid lines and shaded regions show best-fit models and 1σ uncertainties. We also show sizes without the CRISTAL dataset when the fittings have converged. (gray points and solid lines).

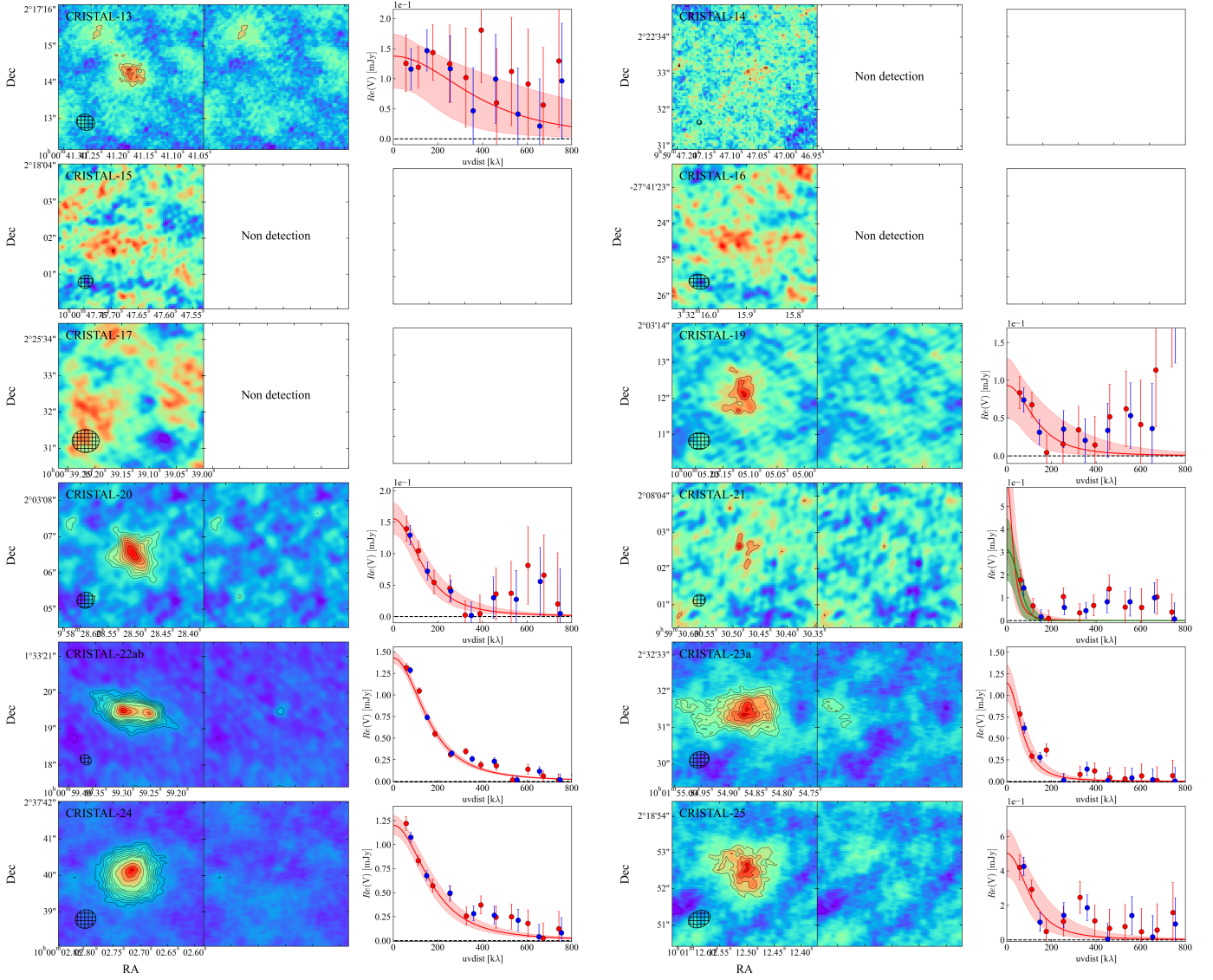


Fig. E.2. Continue from Figure E.2. For CRISTAL-21, we also show the best-fit profile assuming Gaussian to illustrate how the measurement is uncertain due to the extrapolation toward the uv distance of $< 50 k\lambda$

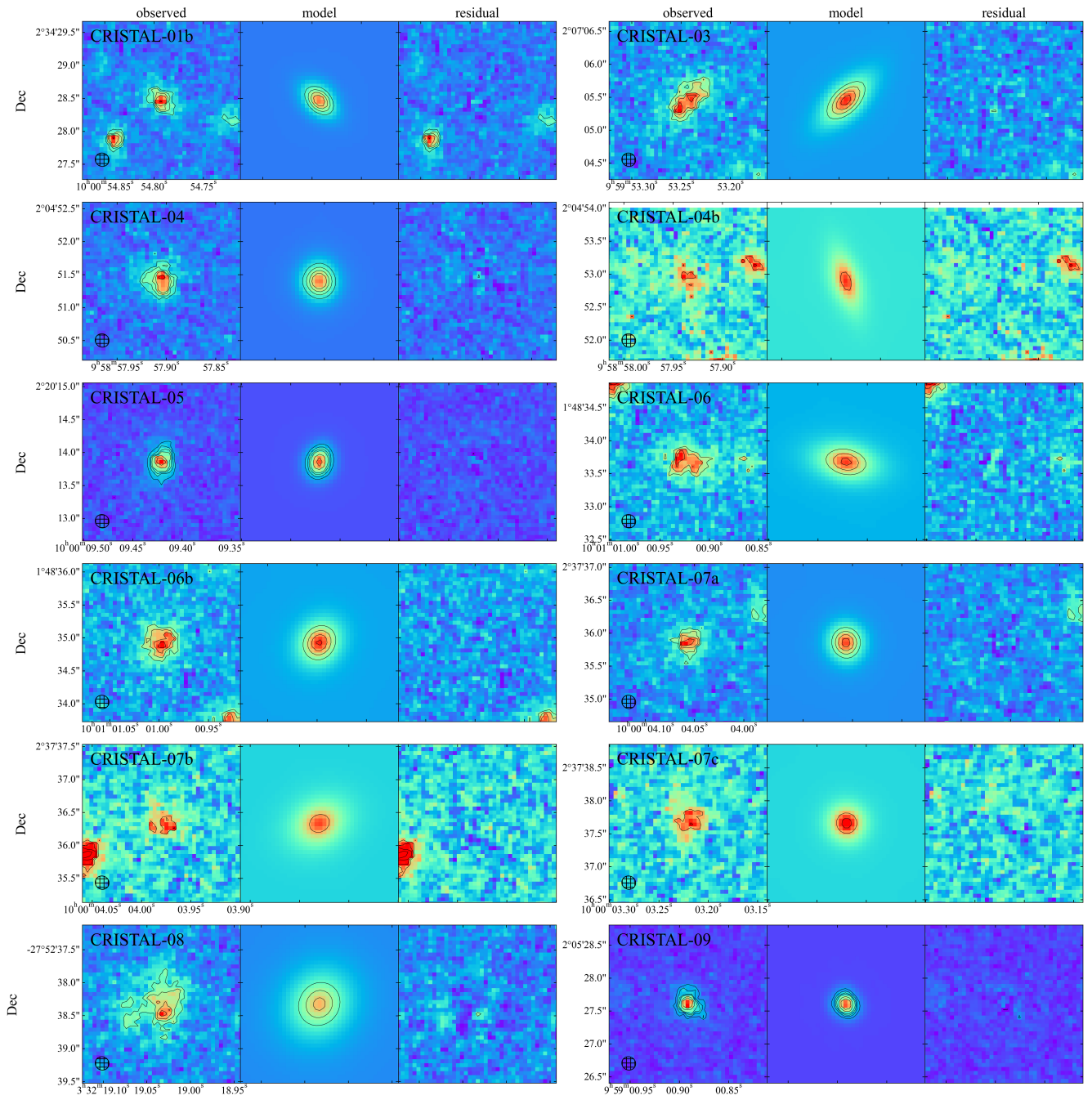


Fig. E.3. The fitting results of the *HST*/F160W images. Observed, model, and residual images are shown from left to right. The contours indicate every 2σ from $\pm 4\sigma$.

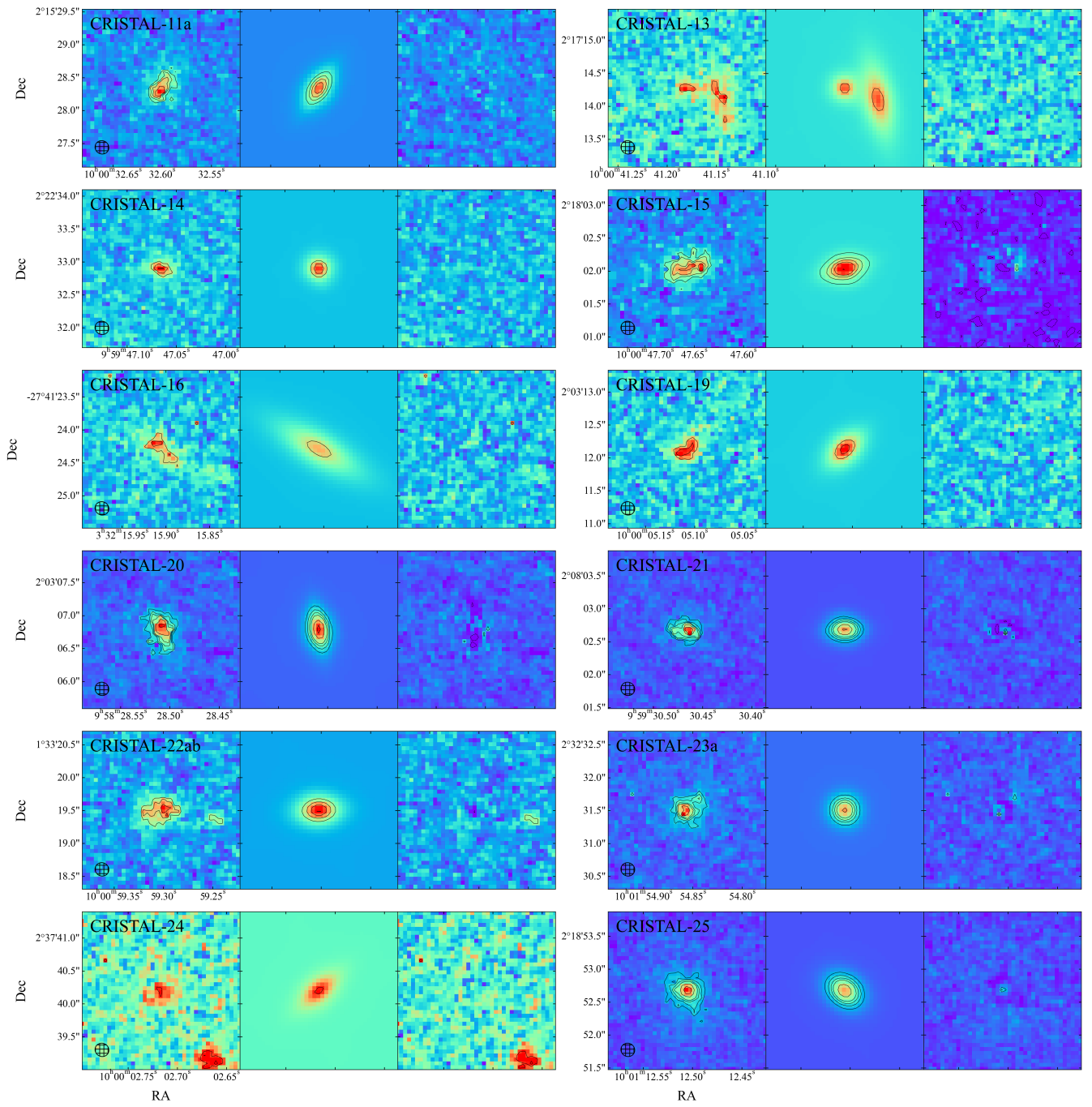


Fig. E.4. (continue)

References

- Algera, H. S. B., Inami, H., Oesch, P. A., et al. 2023, *MNRAS*, 518, 6142
 Arata, S., Yajima, H., Nagamine, K., Li, Y., & Khochfar, S. 2019, *MNRAS*, 488, 2629
 Bakx, T. J. L. C., Sommovigo, L., Carniani, S., et al. 2021, *MNRAS*, 508, L58
 Barnes, J. E. & Hernquist, L. 1996, *ApJ*, 471, 115
 Barro, G., Kriek, M., Pérez-González, P. G., et al. 2016, *ApJ*, 827, L32
 Behrens, C., Pallottini, A., Ferrara, A., Gallerani, S., & Vallini, L. 2018, *MNRAS*, 477, 552
 Béthermin, M., Accard, C., Guillaume, C., et al. 2023, arXiv e-prints, arXiv:2311.08474
 Béthermin, M., Daddi, E., Magdis, G., et al. 2015, *A&A*, 573, A113
 Béthermin, M., Fudamoto, Y., Ginolfi, M., et al. 2020, *A&A*, 643, A2
 Béthermin, M., Wu, H.-Y., Lagache, G., et al. 2017, *A&A*, 607, A89
 Blain, A. W., Smail, I., Ivison, R. J., Kneib, J. P., & Frayer, D. T. 2002, *Phys. Rep.*, 369, 111
 Boquien, M., Burgarella, D., Roehlly, Y., et al. 2019, *A&A*, 622, A103
 Bouwens, R., González-López, J., Aravena, M., et al. 2020, *ApJ*, 902, 112
 Bouwens, R. J., Aravena, M., Decarli, R., et al. 2016, *ApJ*, 833, 72
 Bouwens, R. J., Illingworth, G. D., Blakeslee, J. P., Broadhurst, T. J., & Franx, M. 2004a, *ApJ*, 611, L1
 Bouwens, R. J., Illingworth, G. D., Franx, M., & Ford, H. 2007, *ApJ*, 670, 928
 Bouwens, R. J., Illingworth, G. D., Oesch, P. A., et al. 2012, *ApJ*, 754, 83
 Bouwens, R. J., Smit, R., Schouws, S., et al. 2022, *ApJ*, 931, 160
 Bouwens, R. J., Thompson, R. I., Illingworth, G. D., et al. 2004b, *ApJ*, 616, L79
 Bowler, R. A. A., Bourne, N., Dunlop, J. S., McLure, R. J., & McLeod, D. J. 2018, *MNRAS*, 481, 1631
 Bowler, R. A. A., Cullen, F., McLure, R. J., Dunlop, J. S., & Avison, A. 2022, *MNRAS*, 510, 5088
 Bowler, R. A. A., Inami, H., Sommovigo, L., et al. 2023, arXiv e-prints, arXiv:2309.17386
 Bruzual, G. & Charlot, S. 2003, *MNRAS*, 344, 1000
 Calzetti, D., Armus, L., Bohlin, R. C., et al. 2000, *ApJ*, 533, 682
 Capak, P. L., Carilli, C., Jones, G., et al. 2015, *Nature*, 522, 455
 Casey, C. M., Kartaltepe, J. S., Drakos, N. E., et al. 2022, arXiv e-prints, arXiv:2211.07865
 Casey, C. M., Narayanan, D., & Cooray, A. 2014, *Phys. Rep.*, 541, 45
 Casey, C. M., Zavala, J. A., Aravena, M., et al. 2019, *ApJ*, 887, 55
 Casey, C. M., Zavala, J. A., Manning, S. M., et al. 2021, *ApJ*, 923, 215
 Chabrier, G. 2003, *PASP*, 115, 763
 Chen, C.-C., Smail, I., Swinbank, A. M., et al. 2015, *ApJ*, 799, 194
 Cochrane, R. K., Anglés-Alcázar, D., Cullen, F., & Hayward, C. C. 2023, arXiv e-prints, arXiv:2310.08829
 Cullen, F., McLure, R. J., Khochfar, S., Dunlop, J. S., & Dalla Vecchia, C. 2017, *MNRAS*, 470, 3006
 Czekala, I., Loomis, R. A., Teague, R., et al. 2021, *ApJS*, 257, 2
 da Cunha, E., Walter, F., Smail, I. R., et al. 2015, *ApJ*, 806, 110
 Daddi, E., Cimatti, A., Renzini, A., et al. 2004, *ApJ*, 617, 746
 Daddi, E., Renzini, A., Pirzkal, N., et al. 2005, *ApJ*, 626, 680
 Dale, D. A. & Helou, G. 2002, *ApJ*, 576, 159
 De Breuck, C., Williams, R. J., Swinbank, M., et al. 2014, *A&A*, 565, A59
 Dekel, A., Sari, R., & Ceverino, D. 2009, *ApJ*, 703, 785
 Dessauges-Zavadsky, M., Ginolfi, M., Pozzi, F., et al. 2020, *A&A*, 643, A5
 Devereaux, T., Cassata, P., Ibar, E., et al. 2023, arXiv e-prints, arXiv:2311.11493
 Díaz-Santos, T., Armus, L., Charmandaris, V., et al. 2017, *ApJ*, 846, 32
 Draine, B. T. & Li, A. 2007, *ApJ*, 657, 810
 Dudzevičiūtė, U., Smail, I., Swinbank, A. M., et al. 2020, *MNRAS*, 494, 3828
 Dunlop, J. S., Abraham, R. G., Ashby, M. L. N., et al. 2021, PRIMER: Public Release IMaging for Extragalactic Research, JWST Proposal. Cycle 1, ID. #1837
 Dunlop, J. S., McLure, R. J., Biggs, A. D., et al. 2017, *MNRAS*, 466, 861
 Faisst, A. L., Fudamoto, Y., Oesch, P. A., et al. 2020a, *MNRAS*, 498, 4192
 Faisst, A. L., Schaerer, D., Lemaux, B. C., et al. 2020b, *ApJS*, 247, 61
 Ferguson, H. C., Dickinson, M., Giavalisco, M., et al. 2004, *ApJ*, 600, L107
 Ferland, G. J., Korista, K. T., Verner, D. A., et al. 1998, *PASP*, 110, 761
 Ferrara, A., Hirashita, H., Ouchi, M., & Fujimoto, S. 2017, *MNRAS*, 471, 5018
 Ferrara, A., Sommovigo, L., Dayal, P., et al. 2022, *MNRAS*, 512, 58
 Franco, M., Elbaz, D., Béthermin, M., et al. 2018, *A&A*, 620, A152
 Fudamoto, Y., Oesch, P. A., Faisst, A., et al. 2020a, *A&A*, 643, A4
 Fudamoto, Y., Oesch, P. A., Magnelli, B., et al. 2020b, *MNRAS*, 491, 4724
 Fudamoto, Y., Oesch, P. A., Schouws, S., et al. 2021, *Nature*, 597, 489
 Fujimoto, S., Kohno, K., Ouchi, M., et al. 2023, arXiv e-prints, arXiv:2303.01658
 Fujimoto, S., Ouchi, M., Shibuya, T., & Nagai, H. 2017, *ApJ*, 850, 83
 Fujimoto, S., Silverman, J. D., Béthermin, M., et al. 2020, *ApJ*, 900, 1
 Genzel, R., Burkert, A., Bouché, N., et al. 2008, *ApJ*, 687, 59
 Ginolfi, M., Jones, G. C., Béthermin, M., et al. 2020a, *A&A*, 643, A7
 Ginolfi, M., Jones, G. C., Béthermin, M., et al. 2020b, *A&A*, 633, A90
 Gómez-Guijarro, C., Elbaz, D., Xiao, M., et al. 2022, *A&A*, 658, A43
 Gómez-Guijarro, C., Toft, S., Karim, A., et al. 2018, *ApJ*, 856, 121
 Grupponi, C., Béthermin, M., Loiacono, F., et al. 2020, *A&A*, 643, A8
 Gullberg, B., Smail, I., Swinbank, A. M., et al. 2019, *MNRAS*, 490, 4956
 Guo, Y., Ferguson, H. C., Bell, E. F., et al. 2015, *ApJ*, 800, 39
 Harikane, Y., Ouchi, M., Ono, Y., et al. 2018, *PASJ*, 70, S11
 Hathi, N. P., Jansen, R. A., Windhorst, R. A., et al. 2008, *AJ*, 135, 156
 Herrera-Camus, R., Förster Schreiber, N., Genzel, R., et al. 2021, *A&A*, 649, A31
 Hodge, J. A., Riechers, D., Decarli, R., et al. 2015, *ApJ*, 798, L18
 Hodge, J. A., Swinbank, A. M., Simpson, J. M., et al. 2016, *ApJ*, 833, 103
 Howell, J. H., Armus, L., Mazzarella, J. M., et al. 2010, *ApJ*, 715, 572
 Hygate, A. P. S., Hodge, J. A., da Cunha, E., et al. 2023, *MNRAS*, 524, 1775
 Ikarashi, S., Ivison, R. J., Caputi, K. I., et al. 2015, *ApJ*, 810, 133
 Ikeda, R., Tadaki, K.-i., Iono, D., et al. 2022, *ApJ*, 933, 11
 Inami, H., Algera, H. S. B., Schouws, S., et al. 2022, *MNRAS*, 515, 3126
 Ito, K., Valentino, F., Brammer, G., et al. 2023, arXiv e-prints, arXiv:2307.06994
 Jonsson, P., Groves, B. A., & Cox, T. J. 2010, *MNRAS*, 403, 17
 Kennicutt, Robert C., J. 1998, *ARA&A*, 36, 189
 Kennicutt, R. C. & Evans, N. J. 2012, *ARA&A*, 50, 531
 Laigle, C., McCracken, H. J., Ilbert, O., et al. 2016, *ApJS*, 224, 24
 Lang, P., Schinnerer, E., Smail, I., et al. 2019, *ApJ*, 879, 54
 Laporte, N., Ellis, R. S., Boone, F., et al. 2017, *ApJ*, 837, L21
 Laporte, N., Zitrin, A., Ellis, R. S., et al. 2021, *MNRAS*, 505, 4838
 Le Fèvre, O., Béthermin, M., Faisst, A., et al. 2020, *A&A*, 643, A1
 Leslie, S. K., Schinnerer, E., Groves, B., et al. 2018, *A&A*, 616, A157
 Liang, L., Feldmann, R., Hayward, C. C., et al. 2021, *MNRAS*, 502, 3210
 Lilly, S., Schade, D., Ellis, R., et al. 1998, *ApJ*, 500, 75
 Madau, P. & Dickinson, M. 2014, *ARA&A*, 52, 415
 Magdis, G. E., Daddi, E., Béthermin, M., et al. 2012, *ApJ*, 760, 6
 Magnelli, B., Elbaz, D., Chary, R. R., et al. 2009, *A&A*, 496, 57
 Magnelli, B., Elbaz, D., Chary, R. R., et al. 2011, *A&A*, 528, A35
 Martí-Vidal, I., Vlemmings, W. H. T., Muller, S., & Casey, S. 2014, *A&A*, 563, A136
 McLure, R. J., Dunlop, J. S., Cullen, F., et al. 2018, *MNRAS*, 476, 3991
 Merlin, E., Castellano, M., Santini, P., et al. 2021, *A&A*, 649, A22
 Morishita, T., Stiavelli, M., Chary, R.-R., et al. 2023, arXiv e-prints, arXiv:2308.05018
 Moutard, T., Sawicki, M., Arnouts, S., et al. 2020, *MNRAS*, 494, 1894
 Nelson, E. J., Tadaki, K.-i., Tacconi, L. J., et al. 2019, *ApJ*, 870, 130
 Oesch, P. A., Bouwens, R. J., Carollo, C. M., et al. 2010, *ApJ*, 709, L21
 Ono, Y., Harikane, Y., Ouchi, M., et al. 2023, arXiv e-prints, arXiv:2309.02790
 Pallottini, A., Ferrara, A., Gallerani, S., et al. 2022, *MNRAS*, 513, 5621
 Pannella, M., Carilli, C. L., Daddi, E., et al. 2009, *ApJ*, 698, L116
 Pannella, M., Elbaz, D., Daddi, E., et al. 2015, *ApJ*, 807, 141
 Peng, C. Y., Ho, L. C., Impey, C. D., & Rix, H.-W. 2002, *AJ*, 124, 266
 Popping, G., Pillepich, A., Calistro Rivera, G., et al. 2022, *MNRAS*, 510, 3321
 Popping, G., Puglisi, A., & Norman, C. A. 2017a, *MNRAS*, 472, 2315
 Popping, G., Somerville, R. S., & Galametz, M. 2017b, *MNRAS*, 471, 3152
 Reddy, N. A., Oesch, P. A., Bouwens, R. J., et al. 2018, *ApJ*, 853, 56
 Riechers, D. A., Carilli, C. L., Capak, P. L., et al. 2014, *ApJ*, 796, 84
 Rowan-Robinson, M., Oliver, S., Wang, L., et al. 2016, *MNRAS*, 461, 1100
 Safarzadeh, M., Hayward, C. C., & Ferguson, H. C. 2017, *ApJ*, 840, 15
 Schouws, S., Stefanon, M., Bouwens, R., et al. 2022, *ApJ*, 928, 31
 Schreiber, C., Elbaz, D., Pannella, M., et al. 2018, *A&A*, 609, A30
 Scoville, N., Lee, N., Vanden Bout, P., et al. 2017, *ApJ*, 837, 150
 Sersic, J. L. 1963, Boletín de la Asociación Argentina de Astronomía La Plata Argentina, 6, 41
 Shen, S., Mo, H. J., White, S. D. M., et al. 2003, *MNRAS*, 343, 978
 Shibuya, T., Ouchi, M., Kubo, M., & Harikane, Y. 2016, *ApJ*, 821, 72
 Simpson, J. M., Smail, I., Swinbank, A. M., et al. 2015, *ApJ*, 799, 81
 Skelton, R. E., Whitaker, K. E., Momcheva, I. G., et al. 2014, *ApJS*, 214, 24
 Smail, I., Dudzevičiūtė, U., Stach, S. M., et al. 2021, *MNRAS*, 502, 3426
 Sommovigo, L., Ferrara, A., Carniani, S., et al. 2022a, *MNRAS*, 517, 5930
 Sommovigo, L., Ferrara, A., Carniani, S., et al. 2021, *MNRAS*, 503, 4878
 Sommovigo, L., Ferrara, A., Pallottini, A., et al. 2022b, *MNRAS*, 513, 3122
 Speagle, J. S., Steinhardt, C. L., Capak, P. L., & Silverman, J. D. 2014, *ApJS*, 214, 15
 Spilker, J. S., Marrone, D. P., Aravena, M., et al. 2016, *ApJ*, 826, 112
 Steidel, C. C., Adelberger, K. L., Giavalisco, M., Dickinson, M., & Pettini, M. 1999, *ApJ*, 519, 1
 Tacconi, L. J., Neri, R., Genzel, R., et al. 2013, *ApJ*, 768, 74
 Tadaki, K.-i., Belli, S., Burkert, A., et al. 2020a, *ApJ*, 901, 74
 Tadaki, K.-i., Iono, D., Yun, M. S., et al. 2020b, *ApJ*, 889, 141
 Tadaki, K.-i., Kodama, T., Tanaka, I., et al. 2014, *ApJ*, 780, 77
 Toft, S., Smolčić, V., Magnelli, B., et al. 2014, *ApJ*, 782, 68
 Toft, S., van Dokkum, P., Franx, M., et al. 2007, *ApJ*, 671, 285
 Trujillo, I., Förster Schreiber, N. M., Rudnick, G., et al. 2006, *ApJ*, 650, 18
 Vallini, L., Gallerani, S., Ferrara, A., Pallottini, A., & Yue, B. 2015, *ApJ*, 813, 36
 van der Wel, A., Franx, M., van Dokkum, P. G., et al. 2014, *ApJ*, 788, 28
 Wang, W., Kassin, S. A., Pacifici, C., et al. 2018, *ApJ*, 869, 161
 Ward, E. M., de la Vega, A., Mobasher, B., et al. 2023, arXiv e-prints, arXiv:2311.02162
 Watson, D., Christensen, L., Knudsen, K. K., et al. 2015, *Nature*, 519, 327
 Weaver, J. R., Kauffmann, O. B., Ilbert, O., et al. 2022, *ApJS*, 258, 11
 Whitaker, K. E., Pope, A., Cybulski, R., et al. 2017, *ApJ*, 850, 208
 Witt, A. N. & Gordon, K. D. 2000, *ApJ*, 528, 799
 Wuyts, S., Labbé, I., Förster Schreiber, N. M., et al. 2008, *ApJ*, 682, 985
 Yajima, H., Choi, J.-H., & Nagamine, K. 2011, *MNRAS*, 412, 411
 Yamaguchi, Y., Kohno, K., Hatsukade, B., et al. 2019, *ApJ*, 878, 73
 Zavala, J. A., Casey, C. M., Manning, S. M., et al. 2021, *ApJ*, 909, 165

-
- ¹ Department of Astronomy, The University of Tokyo, 7-3-1 Hongo, Bunkyo, Tokyo 113-0033, Japan
 - ² National Astronomical Observatory of Japan, 2-21-1 Osawa, Mitaka, Tokyo 181-8588, Japan
e-mail: ikki0913astr@gmail.com
 - ³ Faculty of Engineering, Hokkai-Gakuen University, Toyohira-ku, Sapporo 062-8605, Japan
 - ⁴ Department of Astronomical Science, SOKENDAI (The Graduate University for Advanced Studies), Mitaka, Tokyo 181-8588, Japan
 - ⁵ Departamento de Astronomía, Universidad de Concepción, Barrio Universitario, Concepción, Chile
 - ⁶ Instituto de Estudios Astrofísicos, Facultad de Ingeniería y Ciencias, Universidad Diego Portales, Av. Ejército 441, Santiago, Chile
 - ⁷ Sterrenkundig Observatorium, Ghent University, Krijgslaan 281 - S9, B-9000 Ghent, Belgium
 - ⁸ Department of Physics & Astronomy, University College London, Gower Street, London WC1E 6BT, UK
 - ⁹ Max-Planck-Institut für Extraterrestrische Physik (MPE), Giessenbachstr., 85748, Garching, Germany
 - ¹⁰ Las Campanas Observatory, Carnegie Institution of Washington, Casilla 601, La Serena, Chile
 - ¹¹ Department of Physics and Astronomy and George P. and Cynthia Woods Mitchell Institute for Fundamental Physics and Astronomy, Texas A&M University, College Station, TX, USA
 - ¹² Leiden Observatory, Leiden University, NL-2300 RA Leiden, Netherlands
 - ¹³ Joint ALMA Observatory, Alonso de Córdova 3107, Vitacura, Santiago, Chile
 - ¹⁴ National Radio Astronomy Observatory, 520 Edgemont Road, Charlottesville, VA 22903, USA
 - ¹⁵ Jodrell Bank Centre for Astrophysics, Department of Physics and Astronomy, School of Natural Sciences, The University of Manchester, Manchester, M13 9PL, UK
 - ¹⁶ European Southern Observatory (ESO), Karl-Schwarzschild-Straße 2, 85748, Garching bei München, Germany
 - ¹⁷ Centre for Astrophysics and Supercomputing, Swinburne Univ. of Technology, PO Box 218, Hawthorn, VIC, 3122, Australia
 - ¹⁸ ARC Centre of Excellence for All Sky Astrophysics in 3 Dimensions (ASTRO 3D), Australia
 - ¹⁹ Research School of Astronomy and Astrophysics, Australian National University, Canberra, ACT 2611, Australia
 - ²⁰ Institute of Astrophysics, Foundation for Research and Technology-Hellas (FORTH), Heraklion, 70013, Greece
 - ²¹ Chinese Academy of Sciences South America Center for Astronomy (CASSACA), National Astronomical Observatories, CAS, Beijing, 100101, PR China
 - ²² Scuola Normale Superiore, Piazza dei Cavalieri 7, I-50126 Pisa, Italy
 - ²³ Dept. Física Teórica y del Cosmos, Universidad de Granada, Granada, Spain
 - ²⁴ Instituto Universitario Carlos I de Física Teórica y Computacional, Universidad de Granada, E-18071 Granada, Spain
 - ²⁵ Max-Planck Institute for Astrophysics, Karl Schwarzschildstrasse 1, 85748, Garching, Germany
 - ²⁶ INAF - OAS, Osservatorio di Astrofisica e Scienza dello Spazio di Bologna, via Gobetti 93/3, 40129 Bologna, Italy
 - ²⁷ Cavendish Laboratory, University of Cambridge, 19 J.J. Thomson Avenue, Cambridge, CB3 0HE, UK
 - ²⁸ Kavli Institute for Cosmology, University of Cambridge, Madingley Road, Cambridge, CB3 0HA, UK
 - ²⁹ Department of Astronomy and Joint Space-Science Institute, University of Maryland, College Park, Maryland, USA 20742